J. Fluid Mech. (2000), *vol.* 412, *pp.* 21–59. Printed in the United Kingdom

Bubble dispersion and interphase coupling in a free-shear flow

By P. M. RIGHTLEY† AND J. C. LASHERAS

Department of Mechanical and Aerospace Engineering,
University of California, San Diego, CA 92093-0411, USA

(Received 7 July 1998 and in revised form 15 December 1999)

The interaction of a dilute dispersed cloud of microbubbles with a planar free-shear layer is investigated experimentally. The emphasis of this study is on the role of the coherent large scales of the flow in the bubble dispersion field and the energy redistribution within the carrier phase. The interphase momentum transfer integrals that appear in the volume-averaged momentum and energy equations account for redistribution of energy from potential to kinetic within the carrier phase. This results from both the hydrostatic and dynamic pressure fields. The energy redistribution within the carrier phase that is associated with the large-scale structures of the flow possesses significant inhomogeneities within the mixing layer. Peaks of enhanced kinetic energy generation are associated with the upwelling regions at the downstream edge of the coherent vortex cores, and weaker peaks of kinetic energy destruction are associated with downwelling regions. The contribution of the quasi-steady drag term to the total energy redistribution is found to be dominant in only a limited region of the flow field.

1. Introduction

Understanding bubble–fluid interaction in turbulent flows is a keystone in the development of models related to a wide variety of applications. Bubbles are introduced into a flow field intentionally – as in chemical reactors – or inadvertently – as in naval, nuclear reactor or oceanographic systems. Such bubble–fluid interaction often occurs between the flow field and clouds of microbubbles (much smaller than typical flow lengthscales) due to the low residence time of large bubbles. The highly complex nature of the interface between the phases leads to the fact that transfer laws for mass, momentum and energy are difficult to define, and therefore models of the flow require the use of *ad hoc* or empirical closure approximations that may be difficult to justify. More complete and detailed experimental characterization of the fundamental interactions occurring in prototypical bubbly turbulent flows is important for the further evolution of such models.

The importance of large-scale coherent vortical structures in the evolution and entrainment of turbulent two-dimensional free-shear flows was recognized more than two decades ago (Brown & Roshko 1974; Winant & Browand 1974). For a single phase, such flow-fields are well understood and display fundamental characteristics of an anisotropic, inhomogeneous turbulent flow. The interactions of a microbubble cloud with the underlying large-scale structures of the free-shear flow form the basis of this study.

† Present address: Dynamic Experimentation Division, MS P940, Los Alamos National Laboratory, Los Alamos, NM 87545, USA; pright@lanl.gov.

Previous analytical and numerical work involving the dispersion of buoyant particles in free-shear layers (Tio *et al.* 1993*a*; Ruetsch & Meiburg 1993) has indicated that the presence of the large-scale structures will dominate the dispersion of bubbles throughout the shear layer. These studies also suggest that, due to the possible creation of large local void fractions, the underlying flow field itself may be influenced – even for dilute bubble clouds. Detailed experimental studies of the one-way and weak two-way coupling of water droplets in air (Lázaro & Lasheras 1992*a*, *b*; Kiger & Lasheras 1995, 1997) have demonstrated the fundamental role of a particle's Stokes number relative to the large scales in determining dispersion characteristics, and have found peaks of interphase energy transfer away from the region of highest RMS. Other experimental (Lance & Bataille 1991) and numerical (Elghobashi & Truesdell 1993; Druzhinin & Elghobashi 1998) studies noted effects of a dispersed buoyant phase on the slope of the turbulent-energy spectrum at high wavenumbers, for bubble sizes on the order of the Taylor microscale, as well as for microbubbles.

The complexity of the interface for all but the simplest multiphase flows requires the consideration of averaged quantities. The most intuitive averaging method (especially suited to dispersed flows) is volume-averaging (Soo 1989), in which a new lengthscale, the mesoscale, is introduced. Such volume-averaging produces quantitatively similar results to ensemble averaging (Drew 1983). The equations of motion are averaged over this scale and closure comes either in an *ad hoc* fashion or from writing the influence of the actual (complex) interface geometry in terms of mesoscale quantities. In order for the averages over the mesoscales to be smooth functions of time and space, the mesoscale must be larger than the characteristic length of the dispersed phase as well as the interparticle distance. This study considers only dilute, dispersed systems which indicates that the lengthscale of the dispersed phase must be much smaller than the interparticle spacing. Also, for the averaged equations to be meaningful, the mesoscale must resolve the evolution of the flow and thus be sufficiently small compared to the typical flow lengthscales. These restrictions of scale lead to the requirement that

$$D_b \ll \frac{D_b}{\alpha^{1/3}} \ll L_{Meso} \ll L, \tag{1.1}$$

where D_b is a typical dispersed-phase lengthscale (e.g. a bubble diameter), L is a representative flow lengthscale, and α is the volume fraction of the dispersed phase (and therefore $D_b/\alpha^{1/3}$ is a typical interparticle distance). This set of restrictions leads to an upper limit on the typical size of the dispersed phase and to both upper and lower limits on the applicable volume (void) fraction, the latter resulting from the fact that, for representative averages to be computed, sufficient numbers of the dispersed phase must be present (Lázaro & Lasheras 1992*a*, *b*).

Besides satisfying (1.1), small spherical bubbles are also amenable to the application of powerful modern diagnostics, primarily applied to particulate flows up to this time. These diagnostics enable us to characterize the bubbles according to both their size and velocity, and to conditionally average the results to create an ensemble of the two-way coupling between the dispersed phase and the coherent structures of the carrier flow.

2. Experimental facility and diagnostics

2.1. *The facility*

A schematic diagram of the two-layer water channel developed for this study is shown in figure 1. Pumps draw from a large reservoir of water, supplying two head tanks placed on a tower near the inlet to the flow facility. These tanks provide a gravity

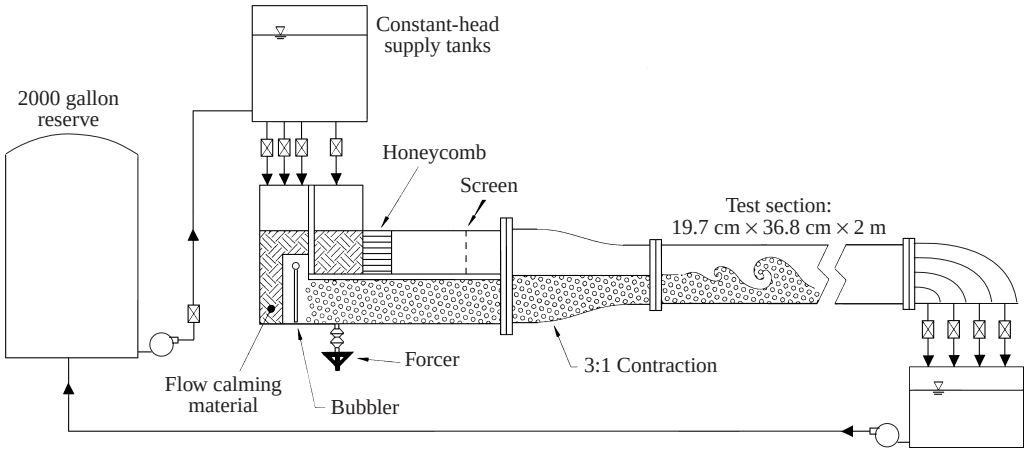

FIGURE 1. Schematic of recirculating water tunnel facility. The tip of the splitter plate is the origin of the (x, y) coordinates with x, the streamwise coordinate, positive downstream, and y, the cross-stream coordinate, positive upward.

feed to the facility while maintaining a constant head. The arrangement enables the water channel to be isolated from the vibrations associated with the supply pumps and to be finely controlled by gate valves. The water channel entrance region is filled with a coarse, open-cell filter foam to damp surface waves. The upper layer is maintained at a lower speed than that of the lower layer and is not laden with bubbles, allowing turbulence-management hardware to be placed there. This hardware consists of a honeycomb flow-straightener, a screen and a 3 : 1 area contraction. Bubbles are injected near the channel entrance in the lower stream, minimizing test-section flow disruption. This precludes a honeycomb or screen being placed within the lower stream as these accumulate bubbles and are detrimental to flow conditioning. Holding tanks at the outflow of the tunnel allow the bubbles time to rise to the surface and be removed so that the bubbles are not recirculated.

The arrangement of the fast stream below the slow stream as well as the placement of the bubbles in the lower stream was necessitated by practical matters. Due to their rise rate, the bubbles were placed in the lower layer so that, when in the test section, the region of the flow nearest the splitter plate would not be free of bubbles. When the lower layer was run at low speeds, significant influence of bubble generation and removal of the flow-control hardware was measured at the test section. In this case the spanwise velocity profile was not flat and the relative turbulence level in the lower stream was very high. This was not the case when the lower stream was run at higher velocities.

Fundamentally, the results of this study would not change if the high-speed stream were the upper layer, and the bubbles were injected in the lower slow-speed stream. This is due to the fact that the shear layer is relatively symmetric (although not entirely). For instance, since the shear layer tends to grow into the low-speed stream, the movement of bubbles vertically upward across the shear layer with the high-speed stream on top would be slightly retarded. This would make only slight quantitative changes in the results presented here.

The flow rate of the lower stream is perturbed sinusoidally by bellows attached to a loudspeaker driven by a function generator and amplifier. The perturbation takes the form of a small cylindrical plug of water being moved into and out of the

lower stream, and amounts to $\approx 0.5\%$ of the layer's volume flux. The fact that the disturbance grows from a small cylindrical region well upstream of the actual mixing layer to encompass the entire spanwise extent of the test section has been verified in an earlier study (Schowalter 1993).

The design requirements for generation of the microbubble clouds were severe: (i) the bubble size distribution must obey the restrictions of scale required for mesoscale averaging detailed in (1.1); (ii) the bubbles should all be smaller than any of the flow lengthscales (i.e. Kolmogorov scale) in order for the equation of motion for an individual bubble to be applicable; (iii) the bubble size distribution must be such that the bubbles are not so large that their rise velocities dominate all flow velocities; (iv) the Weber number of each bubble must remain small throughout the flow field, so that the bubbles will act as rigid and spherical inclusions throughout the test section, enabling optical sizing methods; (v) the bubble generation method must not generate considerable velocity or void fraction inhomogeneities in the laden stream within the test section; and (vi) the bubble generation method cannot significantly change the temperature or other optical properties (e.g. index of refraction) of the laden stream which would then impair the accuracy and applicability of optical flow diagnostics.

A novel bubble-generation device based on the sudden expansion of carbonated water is used. Carbonated water for the experiment is produced by an off-the-shelf soda carbonator. This system pumps deionized water through an atomizer into a chamber pressurized with CO_2 gas. The high surface area of the spray ensures that the water is nearly saturated as it collects at the chamber bottom – a floating switch controls the flow of water into the system. A siphon line then removes the water from the carbonator. In order to eliminate time-dependent bubble generation and to allow larger void fractions than are otherwise possible, it is necessary to utilize a large-volume, constant-pressure carbonated water reservoir. The water in the reservoir never experiences a significant or sudden pressure drop until it reaches the end effector of the bubble generator. The outlet from this vessel was sized so as to prevent sufficient pressure drops that could result in voids forming in the supply line prior to the bubble generator. Also, using non-carbonated water in this reservoir allows duplication of inlet conditions without production of bubbles.

The carbonated water supply feeds a 6.4 mm plenum tube at the bubble generator. From the plenum tube, 20 small (1.6 mm diameter) tubes spaced 25 mm apart extend perpendicularly into the channel. Each of these has four 0.33 mm (#80 wire gauge) holes drilled at 25 mm intervals along its length. The result is an array of micro-nozzles extending uniformly over the cross-sectional area of the channel prior to the contraction. As the carbonated water flows out of these nozzles, the resulting sudden negative pressure step causes homogeneous nucleation of CO_2 bubbles. Rapid mixing with the surrounding, non-carbonated water freezes growth of the bubbles and limits the range of possible bubble sizes.

A summary of the pertinent parameters for this study is presented in table 1.

2.2. *Diagnostics*

The ideal diagnostic for examining this developing flow would provide instantaneous characterizations of the velocity fields of both phases, as well as the dispersion field (including size information) of the dispersed phase over a large field of view. Unfortunately such a diagnostic does not exist in a practical sense. Therefore, in order to provide a detailed characterization of the interaction of the dispersed phase with the large, energy-containing scales of the flow, we utilize conditional averaging techniques in association with point-wise measurements.

Lower free-stream velocity, U_1	$28\,\mathrm{cm\,s^{-1}}$
Upper free-stream velocity, U_2	$6\,\mathrm{cm\,s^{-1}}$
Mean convective velocity, $\overline{U} = \frac{1}{2}(U_1 + U_2)$	$17\,\mathrm{cm\,s^{-1}}$
Perturbation frequency, f	2.1 Hz
Wavelength of Kelvin–Helmholtz billows, $\overline{U}/f$	8 cm
Sauter mean diameter of bubbles, D_{32}	50 μm
Lower free-stream void fraction, α	1×10^{-5}
Typical inter-bubble distance, $D_{32}/\alpha^{1/3}$	$\approx 2\,\mathrm{mm} \approx 50 \times D_{32}$
Bubble Weber number, $We = D_{32}\rho_w U^2/\sigma$	0.02

TABLE 1. Experimental parameters.

It is well known that large-scale Kelvin–Helmholtz billows dominate the dynamics and entrainment of planar free-shear layers (Brown & Roshko 1974; Winant & Browand 1974; Dahm & Dimotakis 1987). It has been seen in several studies (Ho & Huerre 1984; Hussain & Zaman 1980, among others) that forcing the two-dimensional instability can considerably increase the coherency of these large-scale structures. In a study of the developing region of the planar free-shear layer, the dominant nature and repeatability of these large coherent scales in the entrainment and mixing provides a way to produce a complete characterization of the dispersion and velocity fields of both phases through the implementation of conditional sampling techniques. Knowledge is gained of the interactions of the bubble cloud with an ensemble average of such structures. Unfortunately, interactions with smaller scales cannot be quantified with conditional sampling.

These conditional averaging techniques have been found to provide useful information regarding the evolution and dynamics of a variety of free-shear flows (Hussain & Zaman 1980; Antonia 1981; Browand & Weidman 1976) as well as information regarding particle/gas interactions in planar free-shear layers (Lázaro & Lasheras 1992*b*; Kiger 1995). Briefly then, this averaging concept breaks the instantaneous realizations of any measured physical quantity, $\psi(\boldsymbol{x}, t)$, in the flow field into three contributions;

$$\psi(\boldsymbol{x}, t) = \overline{\psi}(\boldsymbol{x}) + \widetilde{\psi}(\boldsymbol{x}, t) + \psi'(\boldsymbol{x}, t). \tag{2.1}$$

These contributions are due to the slowly varying time-average value, $\overline{\psi}(\boldsymbol{x})$, the periodic fluctuations, $\widetilde{\psi}(\boldsymbol{x}, t)$ (for instance, those fluctuations occurring regularly at the forcing frequency and its harmonics), and the random fluctuations (or any fluctuation that is not periodic with the forcing function or its harmonics), $\psi'(\boldsymbol{x}, t)$. The time-average value is defined in the way of traditional turbulence analysis as

$$\overline{\psi}(\boldsymbol{x}) = \frac{1}{T}\int_0^T \psi(\boldsymbol{x}, t)\,\mathrm{d}t \tag{2.2}$$

for some suitably large value of T.

The conditional average used in this study represents the value at a particular location within the forcing period averaged over several periods or structures. For evenly-spaced data, such averaging is easily calculated for each sampling point within a period. However, when the data are obtained at random times (as is the case with PDPA data), the conditional average is computed for bins of finite phase within the forcing period, rather than at a particular point in phase space.

The forcing period, $T_f = f^{-1}$ where f is the forcing frequency, is divided into

N_b phase bins, each of width $\Delta t = T_f/N_b$. Therefore, the conditional average of a physical quantity, $\psi(\boldsymbol{x}, t)$, within phase bin t_i is

$$\langle \psi(\boldsymbol{x}, t_i) \rangle = \frac{1}{N_i} \sum_{1}^{N_i} \psi(\boldsymbol{x}, t_i - \tfrac{1}{2}\Delta t < t < t_i + \tfrac{1}{2}\Delta t), \tag{2.3}$$

where N_i is the total number of points (over all structures) falling within the phase bin and $t_i = (2i-1)(\Delta t/2)$ for $i = 1, 2, \ldots, N_b$.

This phase-average value $\langle \psi(\boldsymbol{x}, t_i) \rangle$ is then equal to the sum of the mean and periodic contributions, i.e. $\langle \psi(\boldsymbol{x}, t_i) \rangle = \overline{\psi}(\boldsymbol{x}) + \widetilde{\psi}(\boldsymbol{x}, t_i - \Delta t/2 < t < t_i + \Delta t/2)$ (Hussain & Zaman 1980). This means that the difference between the instantaneous signal and the phase average is due to the effect of random fluctuations (or, at least, all fluctuations that are not periodic with the forcing frequency or its harmonics), and the difference between the mean and phase average is the result of periodic fluctuations (i.e. fluctuations occurring at the forcing frequency and its harmonics – up to the limit of the finite bin resolution).

Due to the conditional averaging employed, the mesoscale is associated with the phase bins defined in the averaging technique. This allows the use of a point-wise measurement to provide a complete characterization of the velocity fields of both phases as well as the size and dispersion field of the dispersed phase without having poor statistics due to a small number density of the bubbles. Instead we can average over a sufficient number of the passing large-scale Kelvin–Helmholtz billows to produce good statistics at every point in the flow.

The geometry of the line-of-sight laser attenuation instrument used to estimate bubble void fractions is shown in figure 2. This well-characterized technique (Lázaro 1989; Kiger 1995; Rightley 1995) takes the output of a low-power (5 mW) helium-neon laser, passes it through a spatial filter (pinhole), a beam expander and a 3 mm circular orifice, and measures the resulting intensity of the beam after passing through the test section (with and without bubble injection) with a single photodiode (United Detector Technology, PIN-6D shielded by a 5.012% transmittance Melles Griot neutral density filter) on the opposite side. The output of the photodiode is amplified and low-pass filtered before being digitized by a LeCroy 8212A Data Logger.

For pure scattering through a homogeneous medium, it is possible to write down Bouguer's extinction law (Van de Hulst 1957; Siegel & Howell 1981) as

$$\frac{I}{I_0} = \mathrm{e}^{-\Gamma L} \Rightarrow \ln(I/I_0) = -L \sum_i N_i \frac{\pi D_i^2}{2}, \tag{2.4}$$

where I/I_0 is the ratio of the intensity falling on the photodiode with and without the presence of the dispersed phase, Γ is the total extinction cross-section per unit volume in the medium and L is the path-length through the medium.

Introducing the instantaneous probability density function, $f(D_i)$, which represents the fraction of the total dispersed-phase volume occupied by size class D_i, it is convenient to write the number concentration of bubbles of size class D_i as

$$N_i = \alpha \frac{f(D_i)}{\left(\frac{1}{6}\pi D_i^3\right)}, \tag{2.5}$$

where α is the volume concentration (i.e. void fraction) of bubbles. Using (2.5) in (2.4) yields an expression relating the measured value of the ratio of intensities to geometric parameters, the void fraction and the size distribution of the dispersed

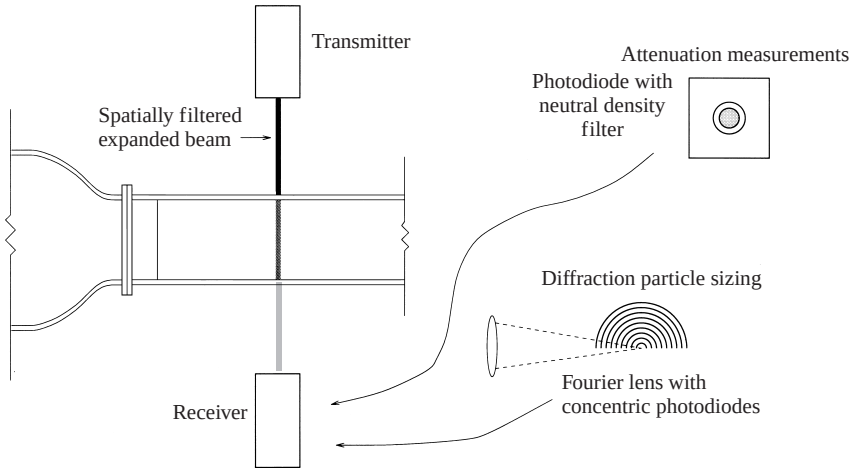

FIGURE 2. Geometry of line-of-sight measurement instruments: laser attenuation/void fraction measurements and diffraction particle sizing.

phase:

$$\ln \frac{I}{I_0} = -3L\alpha \sum_i \frac{f(D_i)}{D_i} = -\frac{3L\alpha}{D_{32}}, \tag{2.6}$$

where

$$D_{32} = \Big(\sum_i N_i D_i^3\Big) \Big/ \Big(\sum_i N_i D_i^2\Big) \tag{2.7}$$

is the Sauter mean diameter of $f(D_i)$. Therefore, the local spanwise-averaged void fraction can be calculated from knowledge of the ratio of beam intensities at the photodiode and the local, instantaneous size distribution (Lázaro & Lasheras 1992*a*, *b*; Kiger & Lasheras 1995; Rightley 1995).

The recent advances in optical particle-sizing technologies have allowed the study of multi-phase flow fields in much greater detail. However, the bulk of the data that have been obtained using and validating these methods have been for particle/gas flows. Two independent sizing methods were investigated: (i) laser-diffraction particle sizing using low angle scattering, and (ii) phase Doppler anemometry (PDPA) using high angle scattering to verify the sizing accuracy of the two instruments. The detailed comparison of the two instruments is presented elsewhere (Rightley 1995).

The geometry of the Malvern 1200HSD laser diffraction particle-sizing instrument is similar to that for laser attenuation (see figure 2), except that the receiver uses a Fourier transform lens and an array of concentric semicircular photodiodes to acquire data. Details of operation and analysis can be found in several sources (for example see Rightley 1995).

The installation of the Aerometrics phase Doppler instrument for this study is depicted in figure 3. This instrument was in a 63° forward-scatter arrangement utilizing the reflection mode dominant at this angle. The output of an Ion Lasers, Inc. Ar^+ laser (total power in both blue and green lines is approximately 700 mW) is driven through a set of fibre optic cables to the 250 mm focal length transmitting lens. The receiver also utilizes a 250 mm focal length lens as well as fibre optic cables to channel the scattered light to the remote photo-multiplier tubes (PMT).

The Aerometrics PDPA system has been calibrated to measure the velocity and

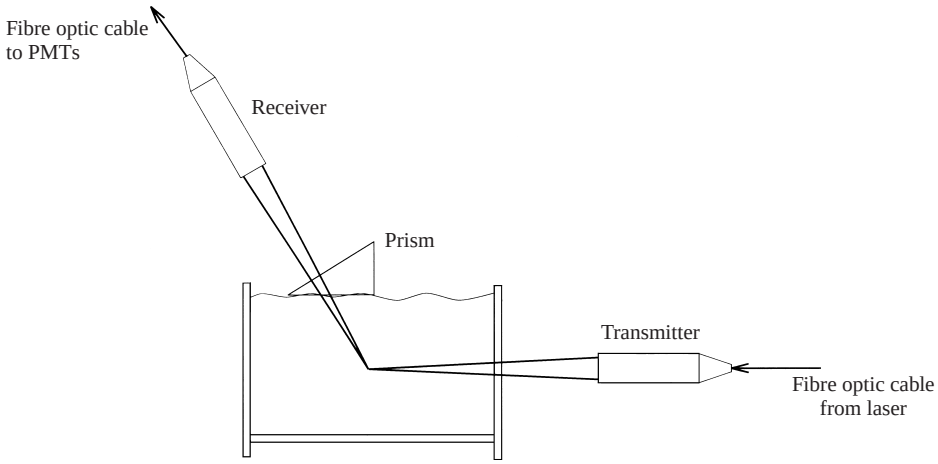

FIGURE 3. Geometry of PDPA measurements. The receiver is positioned to receive 63° forward-scattered light. The prism is used to minimize the distortion of the probe volume seen by the receiver by creating an interface perpendicular to the line-of-sight.

size of spherical particles at several discrete scattering directions. The most useful for studying bubbles is the 63° forward-scattering position. In this position, we are forced to look through the free surface of our water channel. To eliminate the motion of the free surface and the effective distortion resulting from looking through an interface between materials of different refractive index at an angle, we placed a prism on the free surface of the water channel. When investigating bubbly flows, the air–water interface acts approximately as a cylindrical lens when viewed at an angle. To remove the distortion of the probe volume caused by this, both the transmitter and receiver need to be oriented perpendicular to air–water (or air–Plexiglas) interfaces (Aerometrics 1994).

Three PMTs (and their necessary burst analysers) are used in the direction of the green beams, providing the spatial frequency needed to determine size, and a fourth PMT is devoted to the cross-stream velocity. The nominal probe volume of this arrangement is an ellipsoid with axes of approximately $a = b = 80\,\mu\text{m}$ and $c = 2\,\text{mm}$. However, the PDPA receiver utilizes a spatial filter (slit), reducing the volume to an approximately cylindrical shape with dimensions $80\,\mu\text{m} \times 80\,\mu\text{m} \times 300\,\mu\text{m}$. Effective probe volume size, however, depends on several factors including individual particle size and whether both components of velocity are being investigated simultaneously (due to imperfect alignment of four beams through the Plexiglas walls of the water channel). A more complete discussion of these issues is presented elsewhere (Rightley 1995).

Briefly, it is found that the comparison for the volume mean diameters measured by the PDPA and the laser-diffraction particle sizer agree very well, generally within 5% or less. The Sauter mean diameters measured by the two techniques agree to within 10%. Using measured values of the attenuation parameter, $\ln(I_0/I)$, from the laser attenuation instrument with the measured size distribution from both the PDPA and the diffraction particle-sizing instrument, we estimate the void fraction in the free stream at the end of the splitter plate to be 1.0×10^{-5} with an uncertainty of 12% (Rightley 1995). Since there is not significant size segregation of the bubbles within the flow field, the attenuation parameter will be related by a constant to the void fraction of bubbles everywhere in the flow from equation (2.6). We will present

measured values of the attenuation parameter, not estimates of the local void fraction, throughout this paper.

One can characterize the dynamics of several size classes of bubbles in one test when working with a polydispersed size distribution, provided the means exist to distinguish between the particles based on size. Furthermore, conditional averaging allows the study of the dynamics of the various size classes of bubbles with respect to the large energy-containing scales of the carrier phase. In generating the conditional averages, the time series of bursts acquired by the PDPA system is broken into several phase bins corresponding to different locations within the period of the perturbation. This, combined with the necessity to classify the bubbles into discrete size families or bins, limits the number of bursts over which averages can be performed. In turn, this leads to a commensurate increase in the statistical uncertainty of the mean estimates. It is therefore important to guarantee statistically reliable averages for each size class in every bin.

The smallest size class of bubbles is used to characterize and generate averages for the carrier-phase velocity field. This size class is conservatively required to respond faithfully to fluctuations up to 150 Hz. We find through a spectral analysis of the equation of motion for bubbles in a turbulent carrier (Hjelmfelt & Mockros 1966) that only bubbles smaller than 20 μm can be used. This stringent size limitation leads to a problem in obtaining sufficient statistical convergence of the carrier-phase averages due to the small number of the smallest bubbles.

In order to solve this problem, seed particles of the smallest size class were added to the flow field. The requirements on these particles are stringent: (i) they must be able to follow flow fluctuations (and therefore must have a density close to that of water); (ii) they must be distinguishable by size with the PDPA (and therefore must be spherical); and (iii) in order for simultaneous measurements of bubbles and seed particles to be made, the particles must have optical scattering properties very similar to bubbles (so that the reflective mode dominates and the PMTs do not saturate measuring one phase or the other). The addition of spherical hollow glass spheres (Potter's Industries, Inc. Sphericel 110P8) of sizes that would fit almost entirely into the carrier-phase size class alleviates this statistical convergence problem. The glass–air interface in the interior of these particles does scatter light in a way nearly identically to that of bubbles, and they were able to be sized accurately by the PDPA.

Figure 4 shows two number/size histograms obtained from the PDPA system for both the seeding particles and the bubbles alone. A summary of the pertinent numbers for each of the discrete size classes considered from each of these p.d.f.s is presented in table 2. As averages of the particles within the 'fluid' size class (assumed to closely follow the fluctuations of the carrier phase) are of fundamental importance to this study, the statistical convergence of these averages over the smallest particles must be adequate. As can be seen from figure 4 and table 2, the bubbles alone do a poor job populating the smallest size class, whereas the added Sphericel seed falls nearly entirely into this size class.

The amount of seeding added was determined by the requirement to have sufficiently converged statistics for the fluid size class. The amount of seeding was controlled by adding a set amount of Sphericel to the supply tanks (approximately 1 teaspoon per 500 gallons) and then running the system with complete recirculation to ensure complete mixing. The small size, small volume fraction (relative to the bubble cloud) and neutral density of the seeding particles indicate that any influence on the carrier phase is significantly smaller than that of the dispersed phase.

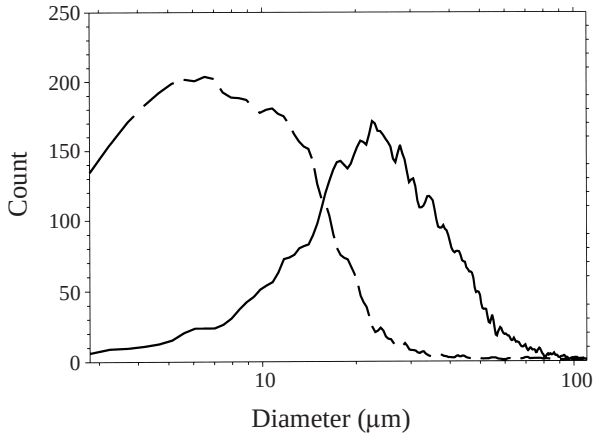

FIGURE 4. Number histograms from PDPA measurements at $x = 10.0\,\text{cm}$, $y = -20.0\,\text{mm}$ for hollow glass spheres (Sphericel) without bubbles present (— —) and for bubbles alone (——).

	Fluid $0 < D < 20\,\mu\text{m}$	Bub. size class 1 $20 < D < 35\,\mu\text{m}$	Size class 2 $35 < D < 65\,\mu\text{m}$	Size class 3 $65\,\mu\text{m} < D$	Total bursts
Sphericel	5695	426	131	41	6293
Bubbles	2870	4424	2996	428	10718

TABLE 2. Contributions of size classes to burst counts over 10 minutes of sampling with the PDPA. Sphericel contributes less than 10% of the counts associated with bubble size classes 1, 2 and 3, yet contributes 66% of the bursts in the fluid size class.

3. Results

3.1. *Mean carrier-phase evolution*

Figure 5 shows the mean profiles of the streamwise velocity from PDPA measurements with Sphericel seed and no bubble injection at various downstream locations. The free-stream velocities are repeatable to 5% for the lower (faster) stream and 10% for the upper stream. This variation occurs between the profiles in figure 5, not within each profile. Our phase-averaged results utilize the data from individual profiles and therefore will not exhibit large repeatability errors. However, repeatability will introduce errors of from 5% to 10% in individual values involving the evolution of quantities downstream. The repeatability of the carrier-phase flow field in the water channel is adequate. Both free-stream regions exhibit flat mean velocity profiles.

The evolution of the level thickness of the streamwise velocity profiles is characterized by the presence of two distinct regions: a nonlinear initial development followed by a linear spreading region downstream of $x/\lambda = 1.25$, $x = 10\,\text{cm}$ (where λ is the most unstable wavelength – and the billow-to-billow distance – 8 cm). Such evolution is typical of the developing region of forced planar mixing layers (Lázaro 1989), but is distinct from the two-region growth seen in studies including the self-similar far field (Liepmann & Laufer 1947; Wygnanski & Fiedler 1970). We define the streamwise momentum integral thickness as

$$\delta_{Iu} = \int_{\infty}^{\infty} z(y)[1 - z(y)]\,\mathrm{d}y, \tag{3.1}$$

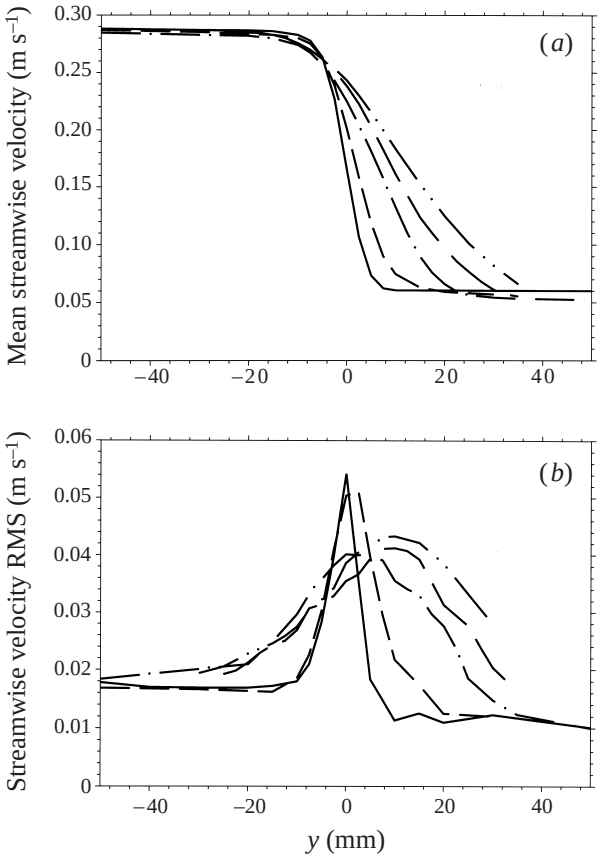

FIGURE 5. Streamwise (*a*) mean and (*b*) RMS velocity profiles for ——, $x/\lambda = 0.31$; — —, $x/\lambda = 0.63$; — · —, $x/\lambda = 1.25$; —— ——, $x/\lambda = 1.88$; and — ·· —, $x/\lambda = 2.50$.

where $z(y) = (u(y) - u(\infty))/(u(\infty) - u(-\infty))$ is the non-dimensional velocity profile normalized with the free-stream velocities. Likewise, we define the level thickness for longitudinal momentum spreading as

$$\delta_{Lu} = y(z = 0.1) - y(z = 0.9). \tag{3.2}$$

Fits to the data observed in this study in the linear spreading region are

$$\delta_{Lu} = 0.134x + 9.1 \text{ and } \delta_{Iu} = 0.021x + 3.3 \tag{3.3}$$

for δ_{Lu}, δ_{Iu} and x in mm. The slope for the level thickness falls on the upper edge of the scatter for the predicted asymptotic growth rate for these free-stream velocities (Weisbrot, Einav & Wygnanski 1982), while the slope of the integral thickness is nearly identical to the far-field growth in another study with similar velocities (Browand & Latigo 1979). Note, however, that forcing the flow significantly enhances growth rates (Lázaro 1989), allowing erroneous interpretations of the flow as self-similar based solely on growth rates.

The computed integral thickness at the measurement station closest to the tip of the splitter plate (i.e. the first station to indicate the complete disappearance of the wake component in the profiles), δ_{Iu_0}, is used as an estimate of the initial momentum thickness. For this study $\delta_{Iu_0} \approx 2.5$ mm. The farthest downstream location considered

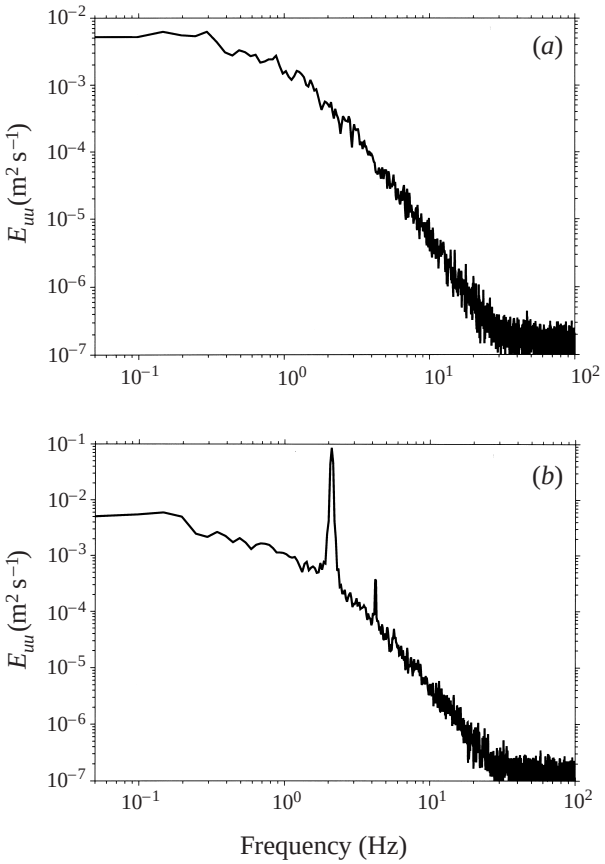

FIGURE 6. Influence of a small single-wavelength perturbation in the lower layer on the streamwise energy spectrum for $x/\lambda = 1.25$ (*a*) without forcing and (*b*) with forcing.

in this study occurs at a non-dimensionalized distance of $x/\delta_{Iu_0} \approx 80$. A significant body of research (see, for example Weisbrot *et al.* 1982; Hussain & Zedan 1978) indicates that the transition to the linear, asymptotic growth rate of the self-similar flow far field occurs for $x/\delta_{Iu_0} = 200$–600 (for unforced flows). Therefore, this study is wholly confined to the developing region of the mixing layer.

The RMS profiles for the streamwise velocity are presented in figure 5(*b*). All of the profiles display only a single peak – a result commonly found for relatively high velocity ratios such as was used in this study (Liepmann & Laufer 1947; Rightley & Lasheras 1996; Lázaro 1989), but different from the two-peaked RMS profiles seen near the tip of the splitter plate for lower velocity ratios but in similar experimental facilities (Winant & Browand 1974; Lasheras, Cho & Maxworthy 1986).

The influence of the low-amplitude forcing system on the streamwise velocity power spectrum is shown in figure 6. No band of frequencies preferred by the shear layer can be discerned from the spectrum presented in the figure in the absence of forcing. However, a perturbation of the high-speed stream with very small amplitudes at $f \approx 2.1$ Hz is seen to greatly increase the coherence of the large-scale (Kelvin–Helmholtz) structures as represented by the large spike introduced into the spectrum. Inviscid linear stability theory of nearly parallel flows provides the formula $St = f_n \delta_{Iu_0}/\overline{U} = 0.032$, where St is the Strouhal number and f_n is the natural frequency (Monkewitz &

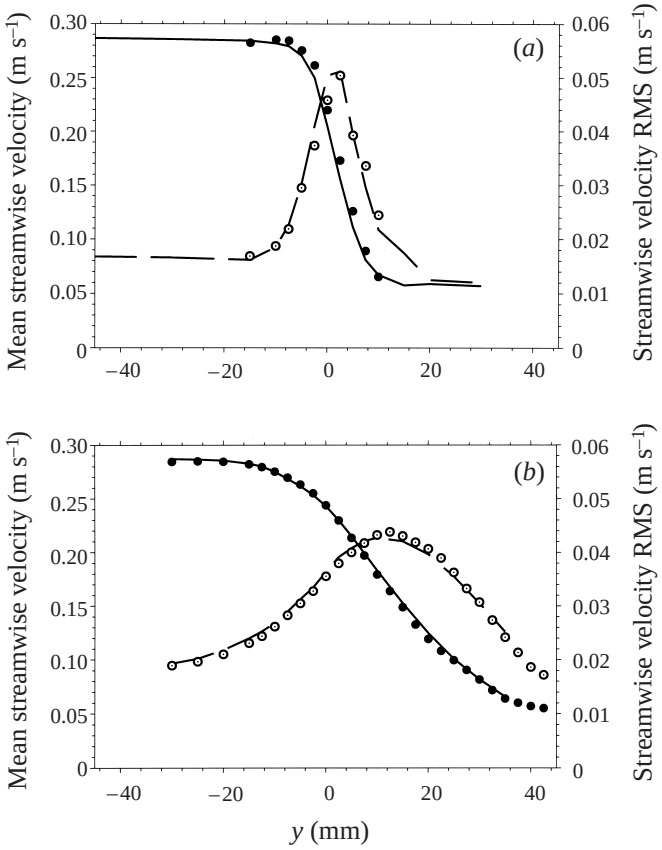

FIGURE 7. Streamwise velocity mean and RMS with and without bubble injection for (*a*) $x/\lambda = 0.63$ and (*b*) $x/\lambda = 2.50$. The solid lines and symbols are the mean velocity profiles without and with bubble injection, respectively. The dashed lines and open symbols are the RMS profiles without and with bubble injection, respectively.

Huerre 1982). The choice of downstream station to be used in determining the value of δ_{Iu_0} appropriate for this formula requires that the wake component of the velocity profile has completely disappeared and is therefore somewhat tenuous (Ho & Huerre 1984). Using $\delta_{Iu_0} = 2.5\,\text{mm}$ and $\overline{U} = \frac{1}{2}(28.8 + 6.0)$, we find $f_n \approx 2.2\,\text{Hz}$. This explains the receptivity of the shear layer to small-amplitude forcing at this frequency.

3.2. *Influence of bubbles on mean carrier-phase evolution*

Little effect of the presence of the dispersed phase is seen on the mean and RMS streamwise velocity profiles of figure 7. The duplication of the inlet conditions was accomplished through the use of the water reservoir and bubble generator injecting either carbonated or non-carbonated water.

Graphs of the influence of the bubble cloud on the mean vertical (cross-stream) velocity profiles are presented in figure 8. Here, an effect is noticeable on the mean values of the cross-stream (vertical) velocity component. The mean vertical velocity is greater everywhere in the presence of bubble injection than without it. However, the RMS profiles are not significantly different with or without bubble injection. Therefore, the bubbles' impact on the mean vertical velocities indicates an increase in

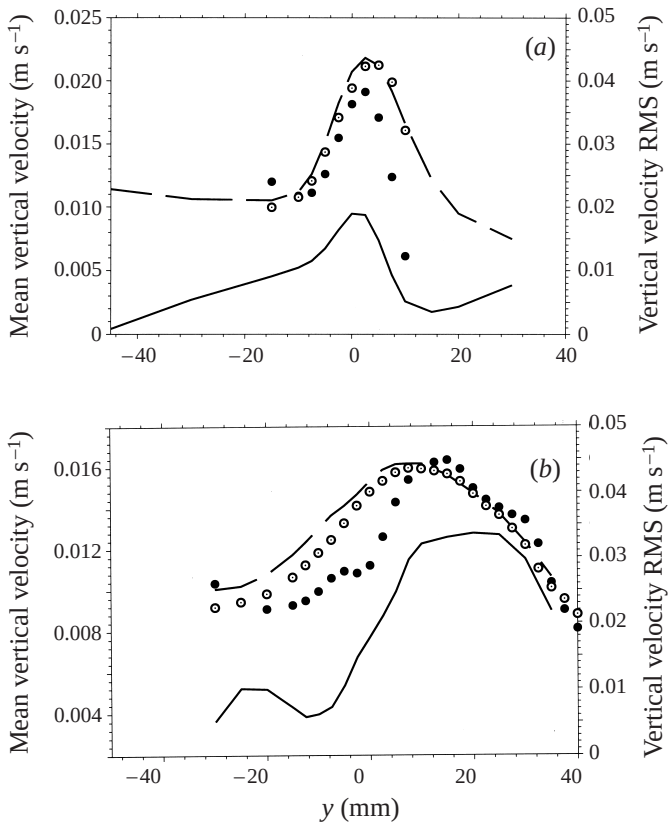

FIGURE 8. Vertical velocity mean and RMS with and without bubble injection for (*a*) $x/\lambda = 0.63$ and (*b*) $x/\lambda = 2.50$. The solid lines and symbols are the mean velocity profiles without and with bubble injection, respectively. The dashed lines and open symbols are the RMS profiles without and with bubble injection, respectively.

the kinetic energy, E_K, of the flow field, but not of the fluctuations as measured by the RMS.

Note that these profiles possess the same shape as those presented by Liepman & Laufer in their seminal 1947 experimental paper on free-shear layers. The fundamental difference is that the experimental velocity profiles under discussion here are entirely positive with no regions of negative flow, whereas Liepman & Laufer's results showed such regions. Such similarities of velocity profile shapes would indicate strongly that the experimental measurements are essentially correct, but with a positive offset velocity. This offset is due to a small drift in the PDPA's Bragg cell frequency. The Bragg cell is used to shift one of the beams of the PDPA by 40 MHz in order to eliminate directional ambiguity.

The full-scale reading for the measurements of the vertical velocities was approximately $1\,\mathrm{m\,s^{-1}}$ (due to limitations of the PDPA instrument). The offset velocity apparent in the mean vertical velocity profiles (when compared to the profiles from Liepman & Laufer) is approximately $4\,\mathrm{mm\,s^{-1}}$. This represents a systematic error of 0.4% of full-scale. The PDPA used to make the measured mean vertical velocity profiles used a variable Bragg cell. The Bragg cells typically used in LDA systems cannot easily be controlled to better than this accuracy without using a fixed-frequency cell.

To reduce the effect of this drift to the minimum possible, the operating temperature of the instrument was ensured to be the same each day that data were taken.

While a systematic error of 0.4% of full-scale is a small error for velocity measurements, when compared to the small velocities present in the cross-stream direction, it becomes significant. The effect of this error is systematic, however, and it does not affect the overall shape of the velocity profile. Small systematic errors like this can be eliminated by shifting of the data in one direction or the other. We wish to present the data as measured to the greatest extent possible. A shift of approximately $4\,\mathrm{mm\,s^{-1}}$ in the vertical velocities will slightly intensify the total E_K destruction regions (presented later) and slightly reduce the total E_K generation regions. The results for the E_K generation due to the drag term will remain the same.

The difference between the mean vertical velocities with and without bubble injection can be seen to be in the range of 5–$10\,\mathrm{mm\,s^{-1}}$. From rise rate data, only the largest bubbles (i.e. $D_b \approx 100\,\mu\mathrm{m}$) have terminal rise velocities comparable to $5\,\mathrm{mm\,s^{-1}}$. The largest size class of bubbles does not account for a majority of the water displaced by the bubble cloud. Thus, the terminal rise velocity of the bubbles representing a majority of the displaced mass of carrier-phase fluid is significantly lower than $5\,\mathrm{mm\,s^{-1}}$. Therefore, instantaneous carrier-phase entrainment associated with the terminal rise rates of the bubbles (or cross-talk between bursts from the larger bubbles and those representing the carrier phase in the averages) is insufficient to account for the measured increase in the mean vertical velocity.

Consider a unit volume in the bubbly free stream and suppose that the volume of the carrier fluid occupied by the bubbles (which, for a unit volume is represented by the free-stream void fraction, α) 'falls' some distance Δz. For this volume, the change in E_K and potential energy, E_P, (considering only the vertical velocity component, v) can be written as

$$\Delta E_K = \tfrac{1}{2}(1-\alpha)\rho_w|\Delta \boldsymbol{v}|^2 \text{ and } \Delta E_P = \alpha\rho_w|\boldsymbol{g}|\Delta z. \tag{3.4}$$

For the small void fractions present in this study, the energy balance can therefore be approximately expressed as

$$\alpha\rho_w|\boldsymbol{g}|\Delta z = \tfrac{1}{2}\rho_w|\Delta \boldsymbol{v}|^2 \Rightarrow \alpha g \Delta z = \tfrac{1}{2}(\Delta v^2). \tag{3.5}$$

For a change in vertical velocity of $\Delta v = 5\,\mathrm{mm\,s^{-1}} = 0.005\,\mathrm{m\,s^{-1}}$ (say, from rest to an approximate terminal rise velocity), and taking the measured free-stream value of $\alpha = 1.5 \times 10^{-5}$, we find $\Delta z \approx 8\,\mathrm{cm}$. The time it takes for the bubbles to travel from the bubble injector to the tip of the splitter plate is approximately 30 s. In this amount of time, a $70\,\mu\mathrm{m}$ bubble – which would be in largest size class – could settle $\approx 8\,\mathrm{cm}$ based on its terminal rise velocity. The energetics of the flow field make it look feasible for the increase in the mean E_K of the carrier-phase velocity field to come from the loss of E_P due to bubble settling. However, this would also suggest that more significant inhomogeneities are present in the lower-free-stream void fraction than are observed.

3.3. *Mean dispersed-phase evolution*

Time-averaged 90° light-scattering flow visualization of the mixing layer both with forcing and without is depicted in figure 9. The tip of the splitter plate is at the left edge of both images and the farthest downstream extent is approximately $x/\lambda = 2.5$.

For the case with forcing, the upper edge of the shear layer can be seen to grow slowly in an induction region immediately downstream of the splitter plate, followed by a more rapid growth rate. After this region of high growth, an inflection point signifies a slowing of the growth rate in the region far downstream of the splitter

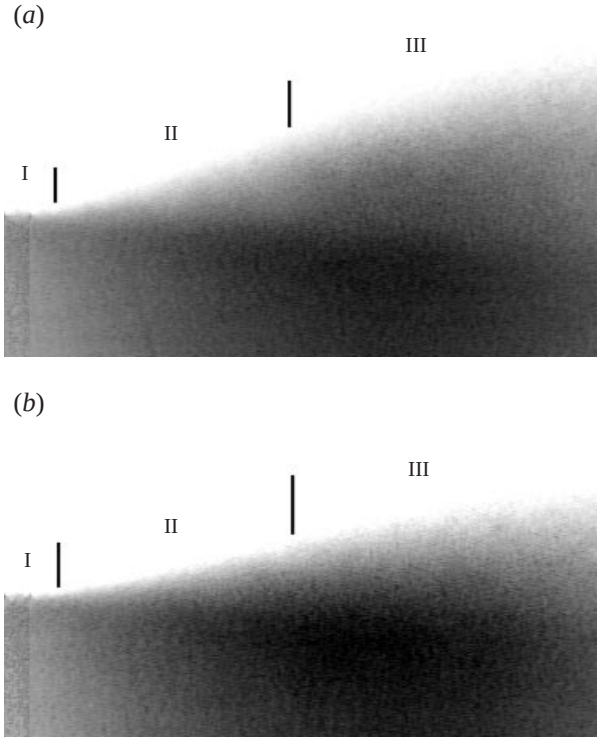

FIGURE 9. Time-averaged flow visualization using 90° scattered light for the (*a*) forced and (*b*) unforced experiments. The tip of the splitter plate is at the left edge of both images and the downstream extent is about $x/\lambda = 2.5$. The region denoted I is the initial induction region, while regions II and III are high- and lower-growth-rate regions, respectively.

plate. As expected for the lateral spread of the carrier-phase velocity field (Dimotakis 1987), the growth of the global bubble dispersion field is directed primarily into the slow-speed stream – which results from the preferential entrainment of fluid from the high-speed side of such mixing layers.

The time-averaged flow visualization of the void fraction evolution for the unperturbed mixing layer illustrates that the lateral spread of the bubble cloud is significantly reduced compared to the layer with perturbation. However, the initial induction and positive sign of curvature regions appear to extend similar distances downstream, followed by an inflection point and a commensurate slowing of the growth rate.

Due to the non-uniform illumination in both the horizontal (due to the light placement) and vertical (due to extinction by the bubble cloud) directions, flow visualization is primarily useful in this investigation only for the qualitative information presented above. A more quantitative measurement utilizes a line-of-sight attenuation instrument. Figure 10 presents the measured time-averaged profiles of the attenuation parameter, $\ln(I_0/I)$, at several downstream measurement stations after normalizing each of the profiles by the value occurring within the lower free stream (i.e. at $y = -30\,\text{mm}$). Notice the appearance of the relatively depleted layer adjacent to the lower free stream at the two farthest downstream measurement stations. This layer is characterized by a significant change in the sign of curvature of the profiles within

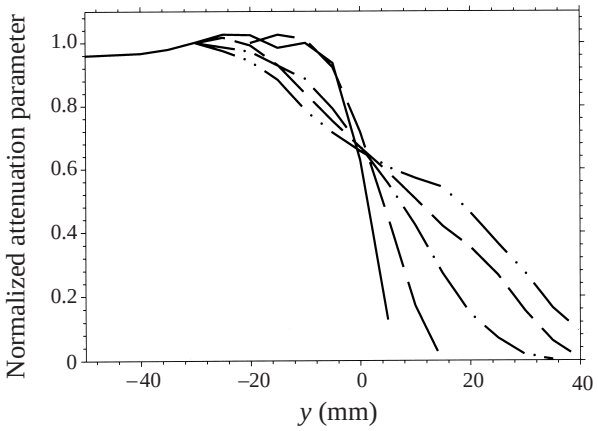

FIGURE 10. Normalized mean attenuation parameter, $\ln(I_0/I)$, profiles for ——, $x/\lambda = 0.31$; — —, $x/\lambda = 0.63$; — · —, $x/\lambda = 1.25$; — —, $x/\lambda = 1.88$; and — · · —, $x/\lambda = 2.50$. This parameter is related to the spanwise-averaged void fraction through Bouguer's law. Notice the development of a depleted sublayer by $x/\lambda = 1.88$.

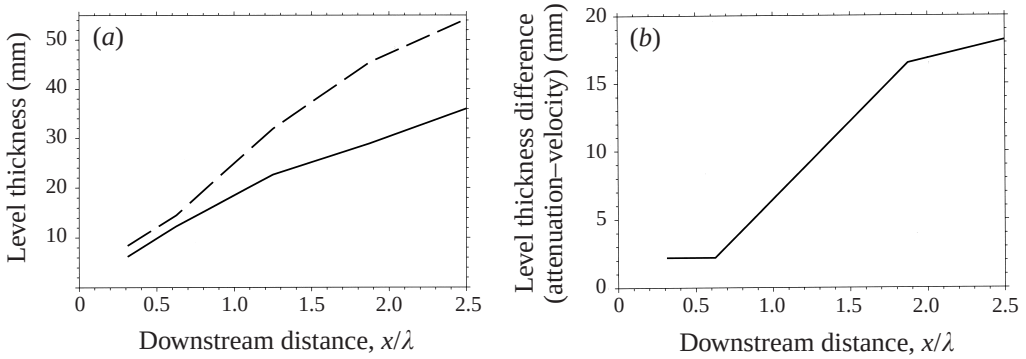

FIGURE 11. Comparison of level thickness growth rates: (*a*) ——, velocity; and — —, attenuation parameter level thicknesses; (*b*) the difference in level thicknesses between the attenuation and velocity fields.

the mixing layer near the lower free stream at $x/\lambda = 1.88$ and 2.5. This change is noticeable to a much lesser degree at $x/\lambda = 1.56$ downstream.

The 10%–90% level thickness measure of the lateral spreading of the bubble dispersion field (figure 11) displays a more rapid growth than that of the mean carrier-phase streamwise velocity profiles. The growth rate of the global void fraction field follows that of the carrier-phase velocity field closely in the initial induction region just downstream of the tip of the splitter plate. Beyond $x/\lambda = 0.63$, the downstream growth rate of the attenuation field increases until approximately the $x/\lambda = 1.25$ measurement station. Between these same stations, however, the spreading rate of the carrier-phase velocity field is already slowing. After the measurement station at $x/\lambda = 1.25$, the growth rate of the attenuation also begins to slow, although it remains greater than the lateral spreading rate of the mean streamwise velocity profiles at all downstream locations. This demonstrates that the bubbles are not acting simply as fluid markers, but that relative motion between the phases can be appreciable. The energetics of this non-negligible slip velocity will be discussed later.

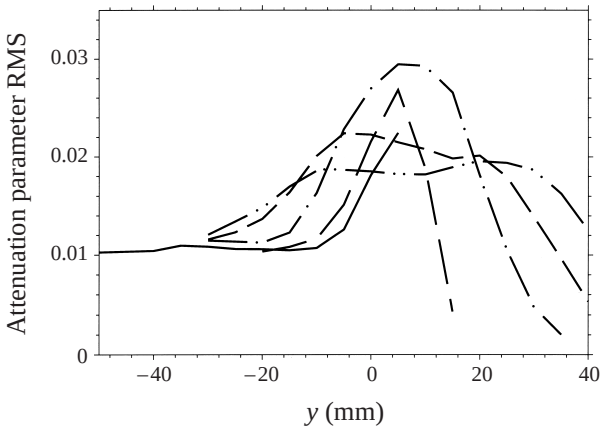

FIGURE 12. Attenuation parameter, $\ln(I_0/I)$, RMS profiles for ——, $x/\lambda = 0.31$; — —, $x/\lambda = 0.63$; — · —, $x/\lambda = 1.25$; —— ——, $x/\lambda = 1.88$; and — ·· —, $x/\lambda = 2.50$.

The difference between the level thicknesses of the mean carrier-phase streamwise velocity profiles and the mean bubble void fraction profiles at each downstream station is also presented in figure 11. A region of significantly enhanced bubble dispersion (compared to the spreading of the streamwise velocity profiles) is distinctly seen from $x/\lambda = 0.63$ to $x/\lambda = 1.88$. In this region, the void fraction field grows $(16.5 - 2.2)/(15.0 - 5.0) = 1.43\,\text{mm per cm}$ of distance downstream. Since the bulk of the level thickness growth is into the upper stream, it makes sense to scale $\delta_L(\text{Attenuation}) - \delta_L(u)$ on the upper-free-stream velocity, $U_2 = 6\,\text{cm s}^{-1}$. The rise velocity of the cloud needed to account for this difference in the level thicknesses as the flow progresses downstream is $V_{T_{Eff}} = 1.43 \times 6 = 8.6\,\text{mm s}^{-1}$– a value more than 1.5 times greater than the rise rate of the largest size bubbles present in the flow field.

After this region of significant enhancement of the void fraction field lateral spreading rate, another region appears in which the growth rate of the bubble dispersion field is still greater than that of the carrier-phase velocity field, but the rate of the divergence of the two curves has decreased. The effective rise rate needed in this region to describe the rate of change of the spreading of the attenuation and velocity fields is $V_{T_{Eff}} = (18.2 - 16.5)/(20.0 - 15.0) \times 6 = 0.34 \times 6 = 2.04\,\text{mm s}^{-1}$. This rise rate corresponds to that of an individual bubble of $D_b = 61\,\mu\text{m}$ which is within the measured size range under consideration.

Therefore, we see that an initial induction region exists just downstream of the tip of the splitter plate where the growth rates of the attenuation and carrier velocity fields are similar, followed by a region of considerably enhanced dispersion of the bubble cloud. In this region, the growth rate of the attenuation field exceeds that due solely to the rise rates of the bubbles. After this, the excess growth of the void fraction field is limited to a rate that can be explained by the rise velocities of at least some of the bubbles present within the cloud. A more detailed analysis of the velocity and dispersion fields that provides an explanation is presented in the next section.

The cross-stream profiles of the attenuation parameter RMS are presented in figure 12. Measurement stations downstream of $x/\lambda = 1.3$ display a bimodal nature with relatively broad, flat regions within the mixing layer. The 'dip' between the two shallow peaks of these latter profiles occurs in the same location as the depleted sublayer seen in the time-averaged flow visualizations (with forcing) and in the mean attenuation profiles.

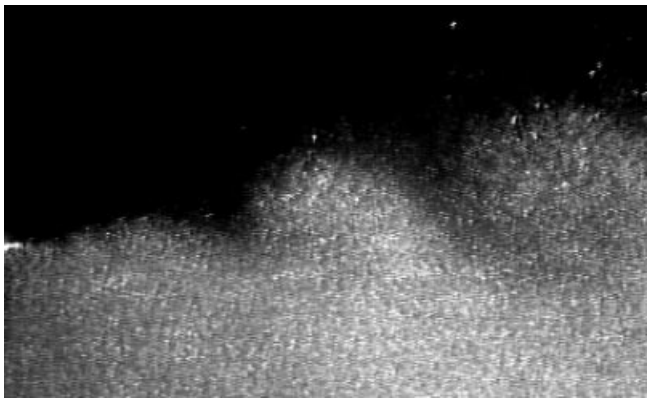

FIGURE 13. Instantaneous visualization – forced flow ($f = 2\,\mathrm{Hz}$) using 90° scattered light. The tip of the splitter plate is at the left edge of the image and the downstream extent is approximately $x/\lambda = 2.5$.

3.4. *Temporal evolution of dispersed phase*

A clear indication of the process by which the depleted sublayer is created is presented in figure 13 showing instantaneous 90° light scattering flow visualization. The image extents are the same as those of figure 9. The bubble cloud is entrained by the fluid entering the mixing region from the high-speed side into the cores of the coherent vortical structures present in the mixing region – this entrainment mechanism has been seen previously (Dimotakis 1987). At the same time, tongues of unladen fluid are entrained into the shear layer from the upper free stream. The significant RMS fluctuations of the attenuation measurements result from the passage of regions of unladen fluid followed by regions laden with bubbles with void fractions nearly equal to those in the lower free stream. As the relative motion of the phases smears the difference in void fraction between these separate regions, the peak RMS values move toward those of the laden free stream.

The depleted sublayer is caused by the subduction of unladen fluid under the vortex cores, as shown by both the instantaneous flow visualization (figure 13) and the superimposed conditionally-averaged carrier-phase velocity and void fraction fields – figure 14. These averages are conditioned on the phase of the forcing function – one period being broken into ten phase bins. To aid in the interpretation of these measurements, two periods of the conditional averages are presented, and the mean convective velocity of the carrier phase has been subtracted. In general, one can identify three distinct regions associated with the conditionally-averaged (or phase-averaged) velocity fields. At the $x/\lambda = 1.88$ measurement station, several distinct topographies can be clearly seen: (i) the centre of the core of the Kelvin–Helmholtz billow at $(\phi, y) = (120°, 9\,\mathrm{mm})$ (and again at $(\phi, y) = (480°, 9\,\mathrm{mm})$ for the other period shown); (ii) the free stagnation point at $(325°, 10\,\mathrm{mm})$; and (iii) the sinusoidal perturbations in the vertical velocities that extend into the lower free stream.

The cores, with relatively high concentrations of bubbles entrained from the lower free stream by the upwelling region which comprises their downstream edge, are separated by depleted regions of unladen fluid entrained from the upper, slower stream more or less into the region near the free stagnation point (i.e. the braid). This unladen fluid is associated with the downwelling fluid on the upstream side of the cores, and is subducted under the core when the Kelvin–Helmholtz billow overturns. This results in the formation of the depleted sublayer adjacent to the

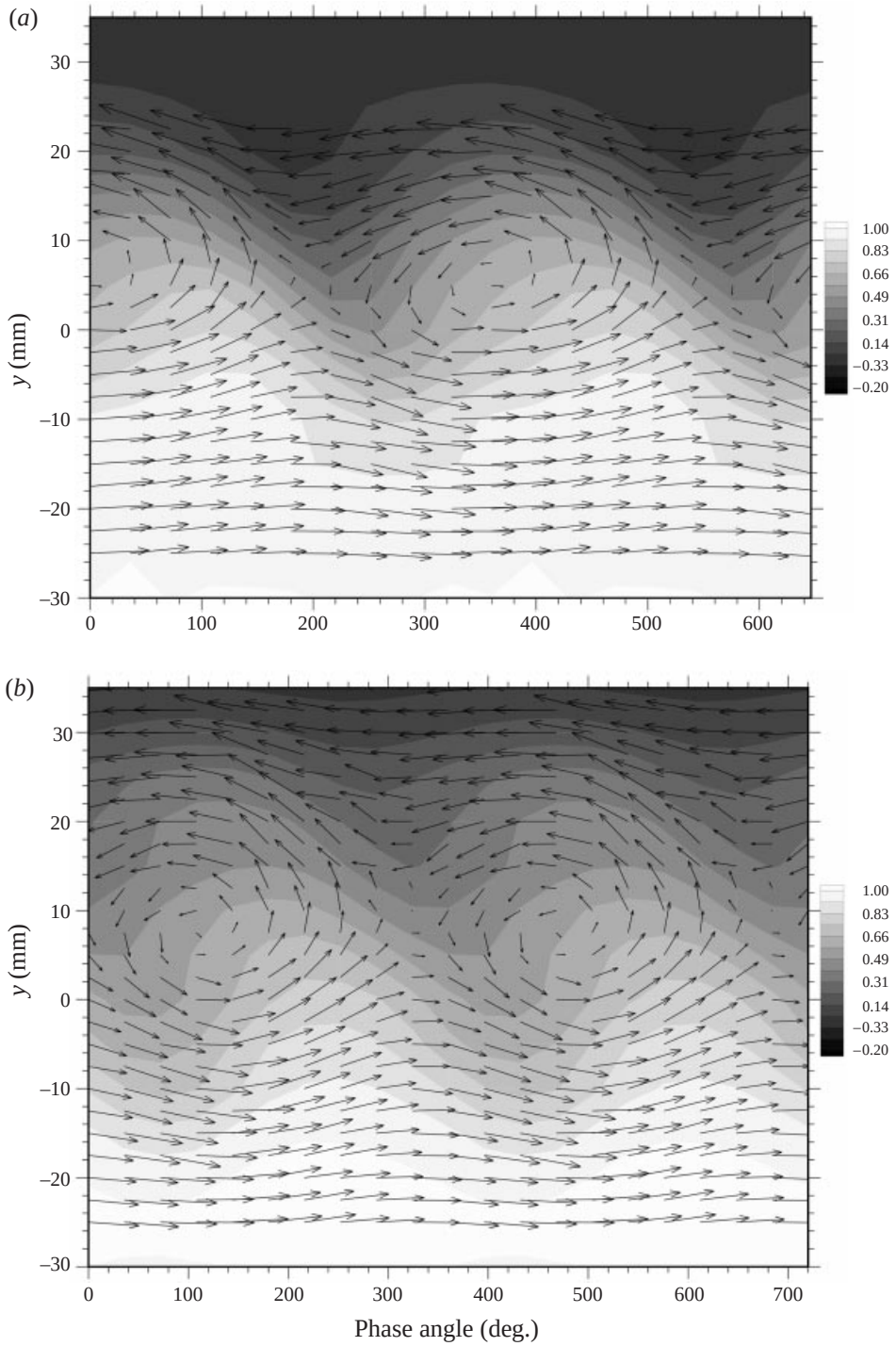

FIGURE 14. Normalized conditionally-averaged attenuation parameter contours and carrier velocity field for (*a*) $x/\lambda = 1.25$ and (*b*) $x/\lambda = 1.88$. The layer's mean velocity of $17\,\mathrm{cm\,s^{-1}}$ has been subtracted from the velocity field. Contour values range from 0 where there are no bubbles (in the upper free stream) to 1.0 in the lower free-stream region.

free-stream. Relative motion of the phases leads to homogenization of this pattern which results from the initial fluid entrainment characteristics and the apparent loss of coherence of the dispersed phase with respect to the large scales of the carrier flow. Yet, even though the peak values of the inhomogeneities of the void fraction field are substantially reduced after the flow has evolved for 2.5 wavelengths, the sublayer associated with the dynamics of the large scales is becoming a more pronounced feature.

The method by which a more homogeneous layer is formed overlaying the relatively depleted sublayer beneath the cores is an effective 'pumping' of bubbles through the mixing layer by the upwelling regions of the flow field. This can be readily seen in the streamtraces of figure 15. These are streamlines, integrated through the measured conditionally-averaged bubble velocity fields, which are also presented in the figures. Note the greater rapidity with which the bubble velocity fields transport the dispersed phase laterally compared to a similarly placed carrier-phase fluid element. As was seen for the global growth of the void fraction field, this enhanced lateral dispersion does not appear to scale simply with the relative rise velocities of the bubbles involved. At $x/\lambda = 1.25$, although the smallest bubble size class is dispersed more rapidly than the carrier phase and less than the other size classes, these larger sizes are dispersed nearly equally. The number-average diameters in each size class are 27, 45 and 85 μm, respectively. These have terminal rise velocities of 0.4, 1.1 and 4.0 mm s^{-1}. The rise velocity of the largest size class is four times that of the next largest size class, yet little difference in the streamtraces is seen at $x/\lambda = 1.25$. This trend is further emphasized at $x/\lambda = 2.50$ where the bubble streamtraces are nearly identical and are substantially different from the dispersion of a fluid element.

Stable accumulation points may exist for buoyant particles near the cores of the large vortical structures present in the mixing layer (Tio *et al.* 1993*b*; Tio & Lasheras 1993; Ruetsch & Meiburg 1993; Sene, Hunt & Thomas 1994). Although a stable accumulation point is known to exist there, we see no apparent increase in the void fraction within the cores of the carrier-phase structures relative to the free-stream void fraction – figure 14. Take the relatively simple vorticity distribution of the modified Rankine vortex as an approximate model of the vorticity in the Kelvin–Helmholtz billows. In this case, the steady velocity field is purely in the azimuthal direction and is given by

$$\boldsymbol{u} = u_\theta = \frac{2U_0(r/R_0)}{1 + (r/R_0)^2}, \tag{3.6}$$

where R_0 is the characteristic dimension of the vortex and U_0 is the value of u_θ at $r = R_0$. For the simulation of a shear layer it is intuitive to take $U_0 = \Delta U/2$ where ΔU is the velocity difference between the streams. The appropriate lengthscale is the wavelength, therefore $R_0 = \lambda$ – the approximate dimension of the large-scale vortical structures. For steady flow, $\mathrm{D}\boldsymbol{u}/\mathrm{D}t = \boldsymbol{u} \cdot \nabla \boldsymbol{u}$, and we have

$$u_\theta = \frac{\Delta U(r/\lambda)}{1 + (r/\lambda)^2} \Rightarrow \boldsymbol{u} \cdot \nabla \boldsymbol{u} = \boldsymbol{u} \cdot \nabla \boldsymbol{u}|_r = -\frac{1}{\lambda} \frac{\Delta U^2(r/\lambda)}{[1 + (r/\lambda)]^2}. \tag{3.7}$$

Utilizing this simplified vorticity model, we consider the competition between the buoyancy forces (resulting from both the static and dynamic pressure fields) and the Stokes drag at the edge of an individual Kelvin–Helmholtz billow (i.e. at $r = \lambda$). These terms are shown in the equation of motion for small spherical particles in a later part of this paper – (4.17). At this location $\mathrm{D}\boldsymbol{u}/\mathrm{D}t \approx \boldsymbol{u} \cdot \nabla \boldsymbol{u}|_r = -(\Delta U)^2/4\lambda$ – representing a pressure force acceleration pointing away from the core. Comparing the magnitude of

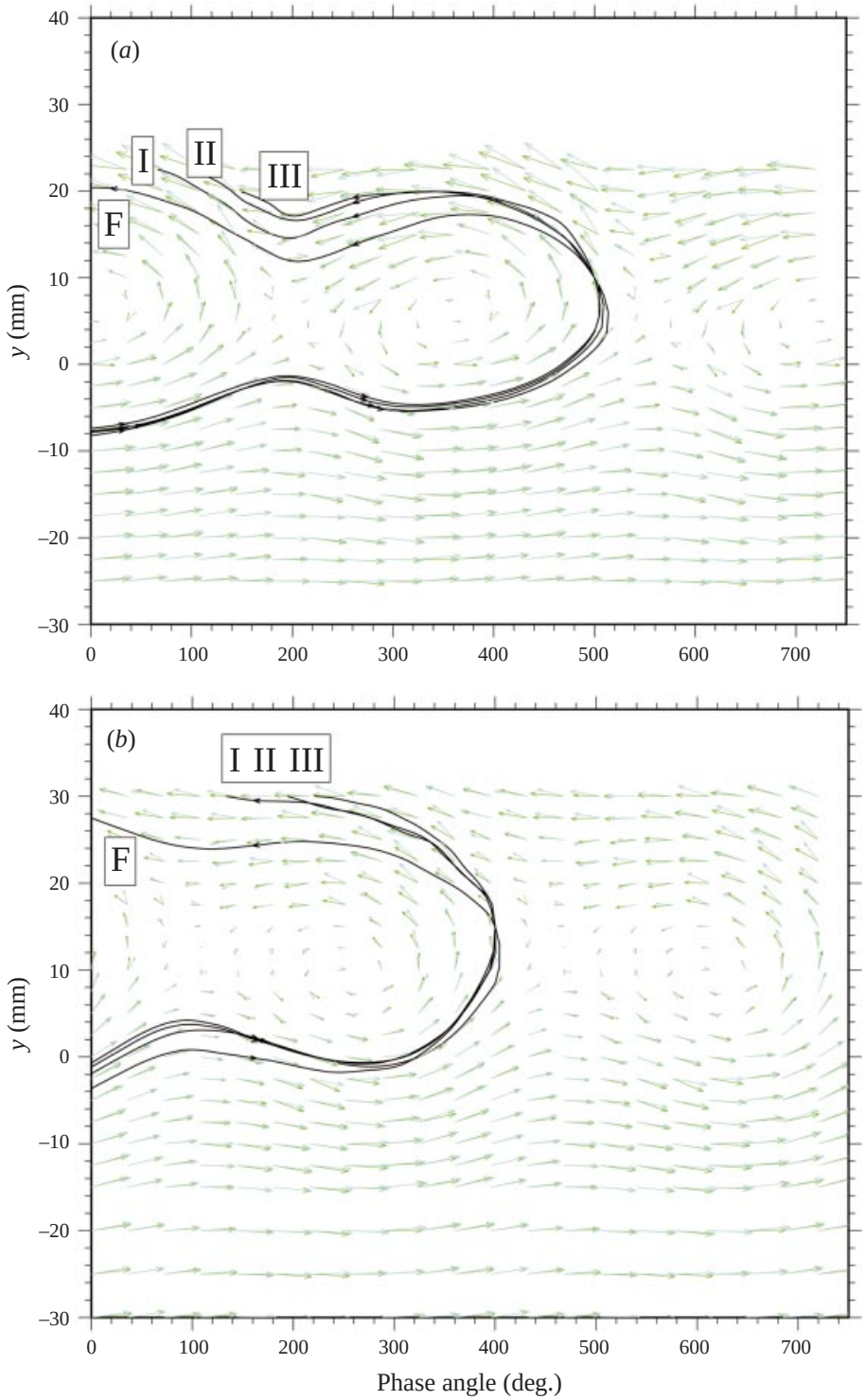

FIGURE 15. For caption see facing page.

the buoyancy force, $F_B = \frac{4}{3}\pi a^3 \rho_w |\boldsymbol{g}|$ (where a is a bubble radius), with that of the drag force, $F_D = 6\pi a \mu_w (\boldsymbol{u} - \boldsymbol{V})$, gives an estimate for the bubbles' terminal rise velocities, V_T. Again, note that previous studies (Detsch 1991; Clift, Grace & Weber 1978) have shown that the quasi-steady Stokes drag law provides accurate estimates for bubbles of the size distribution considered here. Likewise, comparing the magnitude of the pressure ('vortex capture') force, $F_E = -m_w \mathrm{D}\boldsymbol{u}/\mathrm{D}t = -\frac{4}{3}\pi a^3 \rho_w (\Delta U)^2/4\lambda$, with F_D (which, due to the sign change now points toward the centre of the vortex core), gives an estimate for the bubbles' terminal rise and entrainment velocities, V_T and V_E:

$$V_T = \frac{2}{9}\frac{a^2|\boldsymbol{g}|}{v_w} \text{ and } V_E = \frac{1}{18}\frac{a^2(\Delta U^2)}{v_w \lambda}. \tag{3.8}$$

The ratio between these two velocities provides a comparison of the likelihood of bubble entrapment by the vortex through the action of the pressure force to the likelihood of the bubble escaping due to rise velocity associated with the buoyancy force. This ratio is

$$\frac{V_E}{V_T} = \frac{(\Delta U)^2}{4|\boldsymbol{g}|\lambda}. \tag{3.9}$$

Note that this ratio is independent of the size of the bubbles and therefore the relative tendency toward bubble entrapment and escaping through the pull of gravity is uniform for all bubble size classes, though the actual entrainment velocity still depends on the square of the diameter – as does the rise velocity. This result is experimentally apparent in the bubble's temporal dispersion by size, which indicates no clear differentiation in the dispersion of the various size classes.

This entrainment parameter is insensitive to the orientation of the shear layer with respect to gravity (e.g. when the high-speed stream is above or below the low-speed stream). First, note that the entrainment parameter was developed by looking at a cylindrically symmetric vortical flow. Also, when the entrainment parameter becomes large (and therefore entrainment will occur), the dynamic pressure field associated with the local vortex dominates the static pressure field associated with gravity.

This ratio is very similar to the Π parameter suggested previously (Sene *et al.* 1994) not as entrapment parameter, but as the ratio of inertial to buoyancy forces – $\Pi = \Delta U^2/2gx$ where x is the distance downstream from the splitter plate. They chose another parameter, $\Gamma = \Delta U/V_T$ as their entrapment parameter. However, Γ varies inversely with the square of the diameter of the bubble. Although the pressure force scales in this fashion, so does the terminal rise velocity leading to a uniform entrapment ratio across all sizes. The fundamental competition between the buoyancy force tending to make bubbles escape through gravitational settling and the pressure force tending to entrap them near the vortex core would suggest that Π or the ratio V_E/V_T is a more natural entrapment parameter. For large values of V_E/V_T, the pressure force due to the vorticity field of the underlying flow dominates the influence of gravity – leading to significant entrapment of bubbles.

FIGURE 15. Streamtraces integrated through phase-averaged carrier and bubble velocity fields for each size class for (*a*) $x/\lambda = 1.25$ and (*b*) $x/\lambda = 2.50$. The vector fields presented are for the carrier phase (green) and the intermediate bubble size class (cyan). The layer's mean velocity of $17\,\mathrm{cm\,s^{-1}}$ has been subtracted from the velocity fields. The streamtrace labelled F has been integrated through the phase-averaged velocity field of the fluid size class. Likewise, the streamtraces labelled I, II and III have been integrated through the three bubble size class' phase-averaged velocity fields, respectively.

For this study, $V_E/V_T \approx 0.02$ and so we do not expect significant entrapment, due to our limitation of using weak forcing. For the case of weak forcing (and therefore, to some extent, for the naturally developing shear layer), the natural frequency along with the convective velocity, $\overline{U} = \frac{1}{2}(U_1 + U_2)$, determine the typical lengthscale of the Kelvin–Helmholtz billows. The Strouhal number of the most amplified frequency, f_n, is $St_n = 0.032 = f_n \delta_{Iu_0}/\overline{U}$ (Monkewitz & Huerre 1982). Remembering that $\overline{U}/f_n = \lambda$, we see then that $\lambda = \delta_{I_0}/0.032$. For the velocity difference of the shear layer in this work, if the ratio of the entrainment to the rise velocities were to be approximately equal at some locations within the flow field, the initial momentum thickness would need to be $\delta_{I_0} = 40\,\mu\text{m}$! Alas, such a small boundary layer thickness is experimentally impossible to achieve. Were the actual momentum thickness that the channel was able to produce not to change substantially, the required velocity difference would be $\Delta U \approx 2\,\text{m}\,\text{s}^{-1}$ to achieve a value of $V_E/V_T \approx 1$ somewhere within the flow field. This is an order of magnitude greater than that achievable in our facility.

4. Interface energy coupling

4.1. *The form of the interphase coupling*

The analysis of two-phase flow problems is generally complicated by the dissimilar properties of the phases changing across thin interfaces, and by the highly complex boundary geometries. The general approach and formulation of the fundamental equations of motion depend upon the specific flow configuration being studied. Although some relatively general sets of equations exist, there is no formulation that could be considered applicable to all regimes of two-phase flows. Here we use a simple model of the interphase coupling terms for an isothermal incompressible and insoluble cloud of microbubbles in a turbulent flow to gain some understanding of the influence of the dispersed phase on the energetics of the flow.

For the specific case of bubbles embedded within a liquid carrier phase, the assumption of incompressibility must be examined more closely, since it must be assumed that hydrostatic or hydrodynamic pressure changes (and the resulting bubble size fluctuations) are not significant enough to force a relaxation of the incompressibility constraint. In this study, the maximum bubble size variations due to the hydrostatic pressure field is $\approx 0.6\%$ of the bubble's diameter with those variations due to the hydrodynamic pressure field being smaller.

4.2. *General dilute dispersed particulates*

The volume-averaged mesoscale momentum equation for the carrier phase in the limit of a dilute dispersed system is (Rightley 1995; Druzhinin & Elghobashi 1998)

$$\rho_w \frac{\mathrm{D}}{\mathrm{D}t}(\boldsymbol{u}_w) = \nabla \cdot \boldsymbol{T}_w + \rho_w \boldsymbol{g} + \boldsymbol{F}_w, \tag{4.1}$$

where the interphase transfer integral is written as

$$\boldsymbol{F}_w = \frac{1}{V} \int_S \boldsymbol{T}_w \cdot \boldsymbol{n}\, \mathrm{d}S. \tag{4.2}$$

Here, $\boldsymbol{T}$ is the total stress tensor including both the pressure and viscous stresses. Similar equations also hold for the dispersed phase. Closure comes when $\boldsymbol{F}$ can be expressed in terms of mesoscale quantities.

The equation of motion of a small spherical particle or bubble can be written as

(Maxey & Riley 1983; Lovalenti & Brady 1993; Mei & Adrian 1992)

$$m_b \frac{\mathrm{d}\boldsymbol{u}_b}{\mathrm{d}t} = (m_b - m_w)\boldsymbol{g} + m_w \frac{\mathrm{D}\boldsymbol{u}_w}{\mathrm{D}t} - \frac{m_w}{2}\left(\frac{\mathrm{d}\boldsymbol{u}_b}{\mathrm{d}t} - \frac{\mathrm{D}\boldsymbol{u}_w}{\mathrm{D}t}\right) - 3\pi D_b \mu_w (\boldsymbol{u}_b - \boldsymbol{u}_w)$$
$$- \tfrac{3}{2} D_b^2 (\pi \rho_w \mu_w)^{1/2} \int_0^t (t-\tau)^{-1/2} \frac{\partial(\boldsymbol{u}_b - \boldsymbol{u}_w)}{\partial \tau}\, \mathrm{d}\tau \qquad (4.3)$$

where the subscript w denotes the carrier phase, the subscript b denotes the dispersed phase, and $m_w = \frac{1}{6}\pi D_b^3$ is the mass of the carrier phase displaced by the particle or bubble.

Equation (4.3) applies to creeping flow around the individual particles or bubbles with a non-uniform far field. Although this means that the influence of a particle is felt throughout the flow, with the interparticle spacing discussed earlier, the influence of one particle on another is negligible. The maximum Reynolds number associated with the bubbles in this study rising at their terminal rise velocities is less than 0.1. Since the region investigated here is still prior to the mixing transition in the shear layer, the smallest scales of the flow are still large compared to the size of the bubbles themselves. This also is a requirement for the applicability of (4.3).

The decomposition used in formulating (4.3) can be applied in determining the form of the interphase momentum transfer integral for dilute, dispersed systems. The complete flow field external to the sphere is decomposed as the sum of that due to the local carrier-phase flow field in the absence of the particle and that due to the disturbance flow resulting from the relative motion of the particle and the carrier phase, $\tilde{\boldsymbol{u}}(\boldsymbol{x}, t) = \boldsymbol{u}(\boldsymbol{x}, t) + \boldsymbol{u}'(\boldsymbol{x}, t)$. The decomposition applies only on the microscale since the knowledge of the specific flow around each dispersed-phase element is lost on the mesoscale. The sum of the resulting decomposed forces must balance the particle inertia, and therefore

$$m_b \frac{\mathrm{d}\boldsymbol{u}_b}{\mathrm{d}t} = \boldsymbol{f} + \boldsymbol{f}', \qquad (4.4)$$

where the lowercase $\boldsymbol{f}$ is used to denote a single particle, as opposed to the mesoscale-averaged interphase momentum transfer force, $\boldsymbol{F}$. As was done in deriving (4.3), the forces acting on the sphere can be determined as integrals of the stress tensor of the decomposed flow fields over the surface normals (integrals which are of the same form as the interphase momentum transfer integral, (4.2)) or can be converted to volume integrals through Gauss' theorem:

$$\boldsymbol{f} = \int_V \nabla \boldsymbol{T}\, \mathrm{d}V \quad \text{and} \quad \boldsymbol{f}' = \int_V \nabla \boldsymbol{T}'\, \mathrm{d}V. \qquad (4.5)$$

In the limit of dilute dispersed systems, the influence of one particle on another is limited to the cumulative effects on the underlying flow, and the influence of the dispersed phase on the continuous phase is relatively weak (a situation where the restriction on the maximum value of the void fraction, (1.1), proves beneficial). In this limit, to the first approximation, the ambient carrier-phase flow field in the region near an individual particle is governed by the undisturbed momentum equation

$$\rho_w \frac{\mathrm{D}\boldsymbol{u}_w}{\mathrm{D}t} = \nabla \boldsymbol{T}_w + \rho_w \boldsymbol{g} = -\nabla p_w + \mu_w \nabla^2 \boldsymbol{u}_w + \rho_w \boldsymbol{g}. \qquad (4.6)$$

Since the characteristic length of the dispersed phase must also be much smaller than the characteristic lengths for changes in the underlying flow (again from the restriction of scales (1.1)), the flow field can be considered constant over the sphere,

and the integration required in (4.5) over the volume of a single particle gives

$$\boldsymbol{f} = m_w(\mathrm{D}\boldsymbol{u}_w/\mathrm{D}t - \boldsymbol{g}). \tag{4.7}$$

The force acting upon the spherical inclusion within the flow field due to the ambient flow, $\boldsymbol{f}$, is therefore already represented in the equation of motion of the carrier phase. Therefore, to balance the forces acting on the carrier phase at the location of a particle, the mesoscale equation of motion in the weak two-way coupling limit must include a term resulting from the particle's disturbance flow. This can be written as (Rightley 1995)

$$\rho\frac{\mathrm{D}\boldsymbol{u}_w}{\mathrm{D}t} = -\nabla p_w + \mu_w\nabla^2\boldsymbol{u}_w + \rho_w\boldsymbol{g} - \boldsymbol{F}'. \tag{4.8}$$

where the mesoscale-averaged momentum transfer integral is

$$\boldsymbol{F}' = \frac{1}{V}\int_V \boldsymbol{f}'(\boldsymbol{x})\delta(\boldsymbol{x}-\boldsymbol{x}_i)\,\mathrm{d}x = \frac{1}{V}\sum_{i=1}^{N}\boldsymbol{f}'(\boldsymbol{x}_i) \tag{4.9}$$

for $\boldsymbol{x}_i \in V$ and N the number of particles within V. Here $\delta(\boldsymbol{x}-\boldsymbol{x}_i)$ isolates the momentum source resulting from the balance of forces on an individual particle – (4.4) – at each particle location $\boldsymbol{x} = \boldsymbol{x}_i$.

The form of $\boldsymbol{f}'$ in (4.9) can be obtained from $\boldsymbol{f}$ through (4.4), (4.3), and (4.7) and is

$$\boldsymbol{f}' = m_b\boldsymbol{g} - \frac{m_w}{2}\left(\frac{\mathrm{d}\boldsymbol{u}_b}{\mathrm{d}t} - \frac{\mathrm{D}\boldsymbol{u}_w}{\mathrm{D}t}\right) - 3\pi D_b\mu_w(\boldsymbol{u}_b - \boldsymbol{u}_w)$$
$$-\tfrac{3}{2}D_b^2(\pi\rho_w\mu_w)^{1/2}\int_0^t (t-\tau)^{-1/2}\frac{\partial(\boldsymbol{u}_b - \boldsymbol{u}_w)}{\partial\tau}\,\mathrm{d}\tau. \tag{4.10}$$

Other than the single term associated with gravity, all of the terms in the expression for $\boldsymbol{f}'$ result from the relative motion of the particle with respect to the carrier phase.

In this isothermal system, the energy budget can be analysed solely in the context of mechanical energy. Performing the inner product of $\boldsymbol{u}_w$ with (4.1) provides a conservation equation for the E_K of the carrier,

$$\tfrac{1}{2}\rho_w\frac{\mathrm{D}}{\mathrm{D}t}\boldsymbol{u}_w^2 = -\boldsymbol{u}_w\cdot\nabla\boldsymbol{T}_w + \rho_w\boldsymbol{u}_w\cdot\boldsymbol{g} - \boldsymbol{u}_w\cdot\boldsymbol{F}'. \tag{4.11}$$

The influence of the particles on the E_K budget of the underlying flow has the form of the inner product of the force (from the disturbance flow) on the particle and the velocity of the carrier phase. The rate of energy transferred to any body must be the sum of the forces acting upon it dotted with its velocity (i.e. the power transfer to the particle is $(\boldsymbol{f}+\boldsymbol{f}')\cdot\boldsymbol{u}_b$). Note that the power input to the carrier-phase fluid on the mesoscale is not necessarily equal to the power lost by the particle on the microscale or vice versa.

The relative motion of the particle with respect to the underlying flow field will generate motion on the microscale of the bubble – the disturbance flow motion associated with $\boldsymbol{f}'$. This microscale motion represents energy lost by the carrier phase to scales much smaller than the mesoscale. Therefore, the total power lost by the carrier phase in the mesoscale is the sum of the power gained by the particle $(\boldsymbol{f}+\boldsymbol{f}')\cdot\boldsymbol{u}_b$ and the power input into the microscales of the carrier phase due to the disturbance flow.

Thus we see that there are three contributions to the energy input into the carrier phase on the mesoscale. The first is the actual power transferred to the particle as

E_K or $E_P - \sum \boldsymbol{f} \cdot \boldsymbol{u}_b = (\boldsymbol{f} + \boldsymbol{f}') \cdot \boldsymbol{u}_b$. The second, $\boldsymbol{f} \cdot \boldsymbol{u}_b$, represents the conversion of E_P to E_K and vice versa within the carrier phase through the work of the buoyancy and pressure forces. The third, $-(\boldsymbol{u}_w - \boldsymbol{u}_b) \cdot \boldsymbol{f}'$, represents the addition of E_K to the carrier phase on scales much smaller than the mesoscale through the action of the disturbance flow of the particle. This final contribution exists whenever the dispersed and carrier phases possess a relative motion. For the case of heavy particles in a gas (for instance, a spray), the drag term alone often balances the particle inertia (Lázaro 1989; Williams 1960). In such a case, the power transferred to the particle is well defined and the work of the buoyancy forces can be neglected, and since $\boldsymbol{f}'$ depends linearly on the relative velocity between the phases, if there is sufficient slip for $\boldsymbol{f}'$ to become appreciable, the loss of energy to the microscales ($-(\boldsymbol{u}_w - \boldsymbol{u}_b) \cdot \boldsymbol{f}'$) must also be important. Likewise, for a bubble rising in a still liquid, a 'significant' disturbance is created in the liquid (relative to the bubble's mass and therefore its energy). Consider the wake of a 1 cm diameter bubble rising due to gravity. In this case, the wake will possess significant E_K, yet the bubble as it rises neither possesses nor gains energy, because it is essentially massless. Realizing that the pressure field driving the conversion from E_P to E_K may result from either static or dynamic pressure fields, we see that $\boldsymbol{f} \cdot \boldsymbol{u}_b$, where $\boldsymbol{f}$ is expressed in (4.7), is the correct form for the conversion of E_P into E_K at the mesoscale of the carrier phase.

4.3. *Interphase coupling for microbubbles in water*

Further simplifications to the formulation for dilute dispersed two-phase systems exist for bubbles. For the case of massless particles where $m_w = \frac{1}{6}\pi D_b^3 \rho_w \gg m_b = \frac{1}{6}\pi D_b^3 \rho_b$, inertia of the particle is negligible and (4.4) becomes

$$0 = \boldsymbol{f} + \boldsymbol{f}' \Rightarrow \boldsymbol{f} = -\boldsymbol{f}'. \tag{4.12}$$

The momentum equation for the carrier phase, (4.8), under the influence of an individual bubble, can then be written as

$$\rho_w \frac{\mathrm{D}\boldsymbol{u}_w}{\mathrm{D}t} = -\nabla p_w + \mu_w \nabla^2 \boldsymbol{u}_w + \rho_w \boldsymbol{g} + \boldsymbol{F}, \tag{4.13}$$

where

$$\boldsymbol{F} = \frac{1}{V} \int_V \boldsymbol{f}(\boldsymbol{x}) \delta(\boldsymbol{x} - \boldsymbol{x}_i)\, \mathrm{d}\boldsymbol{x} = \frac{1}{V} \sum_{i=1}^{N} \boldsymbol{f}(\boldsymbol{x}_i) \tag{4.14}$$

for $\boldsymbol{x}_i \in V$. Using (4.7), we have

$$\boldsymbol{F} = \rho_w \alpha_b (\mathrm{D}\boldsymbol{u}_w/\mathrm{D}t - \boldsymbol{g}), \tag{4.15}$$

where $\rho_w \alpha_b = (1/V) \sum m_w(\boldsymbol{x}_i)$ is the mass of water displaced by the bubble cloud per unit volume. Therefore, (4.13) can be written equivalently as

$$\rho_w \frac{\mathrm{D}\boldsymbol{u}_w}{\mathrm{D}t} = -\nabla p_w + \mu_w \nabla^2 \boldsymbol{u}_w + \rho_w \boldsymbol{g} + \rho_w \alpha_b \left(\frac{\mathrm{D}\boldsymbol{u}_w}{\mathrm{D}t} - \boldsymbol{g} \right). \tag{4.16}$$

This result for the mesoscale-averaged momentum equation of the carrier phase is similar to that given for a Lagrangian analysis of the influence of individual bubbles on the carrier phase (Maxey, Chang & Wang 1994). The application of mesoscale averaging to that expression is straightforward, resulting in an equation of motion identical to (4.16). With the exception of the influence of the dynamic pressure term $\mathrm{D}\boldsymbol{u}_w/\mathrm{D}t$ on the interphase momentum transfer integral, this expression resembles that of a Boussinesq approximation for buoyancy-driven variable-density flow fields

(Turner 1973). Previous work involving buoyancy effects of particles on shear flows (Ruetsch & Meiburg 1994; Lumley 1976) has used formulations equivalent to the Boussinesq approximation and has neglected the influence of the dynamic pressure contribution.

It is also possible to understand the equation of motion of small bubbles, (4.3), as a balance between the forces due to the ambient flow field and those due to the disturbance flow,

$$m_w\left(\boldsymbol{g}-\frac{\mathrm{D}\boldsymbol{u}_w}{\mathrm{D}t}\right)=3\pi D_b\mu_w(\boldsymbol{u}_b-\boldsymbol{u}_w)+\frac{m_w}{2}\left(\frac{\mathrm{d}\boldsymbol{u}_b}{\mathrm{d}t}-\frac{\mathrm{D}\boldsymbol{u}_w}{\mathrm{D}t}\right)$$
$$+\tfrac{3}{2}D_b^2(\pi\rho_w\mu_w)^{1/2}\int_0^t(t-\tau)^{-1/2}\frac{\partial(\boldsymbol{u}_b-\boldsymbol{u}_w)}{\partial\tau}\,\mathrm{d}\tau. \quad (4.17)$$

The form for the quasi-steady drag term in (4.17) is that for a rigid sphere in the limit of zero Reynolds number (Stokes flow). Analysis of fluid spheres in the Stokes limit suggests the need for a different numerical coefficient due to the circulation within the sphere and motion of the interface. However, work on bubbles rising in water under controlled circumstances suggests that, unless extraordinary measures are taken to purify the water, microbubbles will behave as rigid spheres due to the accumulation of surfactants on the interface (Detsch 1991).

The appropriate form of the pressure term has been debated (Corrsin & Lumley 1956), and the appropriate form of the Bassett history term is under discussion as well (Mei, Adrian & Hanratty 1991). It is important to note that uncertainty in the form of $\boldsymbol{f}'$ is not critical to this analysis due to its simple relationship with $\boldsymbol{f}$ for a bubble. The simple form of $\boldsymbol{f}$ allows it to be measured and yet represent all of the contributions from the disturbance flow field. For instance, the specific form of $\boldsymbol{f}'$ may include a lift term (Auton 1987; Saffman 1985; Mei 1992; Sridhar & Katz 1993), the exact expression of which is still uncertain; however, measuring $\boldsymbol{f}$, we still measure the influence of any unknown lift force.

4.4. *Energy*

Studies of one-way coupling of microbubbles in free-shear layers have produced insight into the relevant physical processes (see Ruetsch & Meiburg 1993; Tio *et al.* 1993*b*; Sene *et al.* 1994, for example). Such studies have relied upon Lagrangian particle tracking techniques – using some form of equation of motion for the individual bubbles similar to (4.17). Substantially greater complexity is involved in two-way coupling studies due to the fact that, not only must the dispersion process be correctly modelled, the momentum and energy interchange across the interface must also be taken into account. To date, the majority of such work has utilized moment-method closures (for example, Viollet & Simonin 1994; Elghobashi & Abou-Arab 1983). Although studies combining particle tracking and two-way coupling effects are gaining prominence (Ruetsch & Meiburg 1994; Elghobashi & Truesdell 1993; Druzhinin & Elghobashi 1998; Squires & Eaton 1990), these have been limited to dispersed phases typified by small characteristic dimensions relative to flow lengthscales and to low overall void fractions.

A massless dispersed phase can possess neither E_P nor E_K. However, a bubble cloud introduced into a quiescent tank of water will rise and induce motion of the carrier phase (water) – even large-scale recirculations with characteristic lengths much greater than the dimensions of the bubbles themselves. Therefore, interphase momentum and E_K effects must exist, but must be represented as a redistribution of energy from E_P

to E_K within the carrier phase. As bubbles 'rise' (either upward through the influence of the hydrostatic pressure field or toward low-pressure regions due to the dynamic pressure field) the carrier phase effectively 'falls' – reducing the E_P of this phase and therefore (by conservation of total energy) increasing its E_K.

From (4.16) and (4.11), the mesoscale interphase momentum transfer integral and the interphase E_K redistribution can be written as

$$\boldsymbol{F} = \rho_w \alpha_b (\mathrm{D}\boldsymbol{u}_w/\mathrm{D}t - \boldsymbol{g}) \text{ and } \boldsymbol{F} \cdot \boldsymbol{u}_w = \rho_w \alpha_b (\mathrm{D}\boldsymbol{u}_w/\mathrm{D}t - \boldsymbol{g}) \cdot \boldsymbol{u}_w. \tag{4.18}$$

Simultaneous accurate measurements of both the bubble dispersion field and the carrier-phase velocity field are beyond the scope of current practical instrumentation. For this reason, we limit ourselves to the influence of the large scales through the use of conditional averaging. These conditional averages will not include the contribution resulting from scales smaller than the Kelvin–Helmholtz billows of the flow or void-fraction fields. Because of this limitation and the small size of the bubbles in this study, we cannot do any more than speculate as to the scales at which energy is generated or removed from the mesoscale. It should suffice to say that, for the energy transfer associated with a microbubble, the scale of interaction is much smaller than the mesoscale.

The most significant fluctuations of both the void fraction and carrier-phase velocity fields are those resulting from these large scales in the developing region of the mixing layer. Downstream development of the flow field leads to diminishing fluctuations of the void fraction field at the forcing frequency. This is due to a smearing of the initially inhomogeneous entrainment into the shear layer – the significant influence of the large scales farther downstream is seen in the growing prominence of the depleted sublayer. Only the influence of small-scale variations of the dynamic pressure field is ignored by the results presented here for the energy redistribution within the carrier phase due to the presence of the bubble cloud.

An estimate of the contribution of the local fluid acceleration to the total energy redistribution in this flow field requires Lagrangian information following fluid particles. The conditionally-averaged velocity field of the carrier phase (presented in figure 14) can be used to provide an estimate of this local carrier phase acceleration, $\mathrm{D}\boldsymbol{u}_w/\mathrm{D}t$, from the convective terms of the substantial derivative alone – that is, let $\mathrm{D}\boldsymbol{u}_w/\mathrm{D}t \approx \boldsymbol{u}_w \cdot \nabla \boldsymbol{u}_w$. This first requires converting the phase angle of each discrete conditional-averaging bin into streamwise distances then numerically differentiating the data to determine $\nabla \boldsymbol{u}_w$.

The computed fluid accelerations are relatively smooth in figure 16. The pressure field results in an acceleration of the fluid toward the core of the large vortical structure at $(\phi, y) = (350^\circ, 5\,\mathrm{mm})$, and, in general, away from the free-stagnation point – i.e. $(\phi, y) = (200^\circ, 5\,\mathrm{mm})$. The maximum magnitudes of these accelerations associated with the large scales can be seen to be only 10% of the acceleration due to gravity. That these accelerations are small compared to gravity is of no surprise since the vorticity distribution of the large scales is relatively diffuse (which is why $V_E/V_T \ll 1$). In fact, over 90% of the energy redistribution comes from forces acting in the vertical direction – even though the carrier-phase velocities in this direction are substantially smaller than in the streamwise direction. Therefore, the use of these computed values for the dynamic pressure field will introduce a relatively small perturbation on the interphase energy redistribution associated solely with gravitational effects.

Estimated values of the interface energy transfer integral, (4.18), within the carrier phase resulting from the entire bubble cloud are presented in figure 17 for the $x/\lambda =$ 1.25 and 2.50 measurement stations. The upwelling region downstream of each vortex

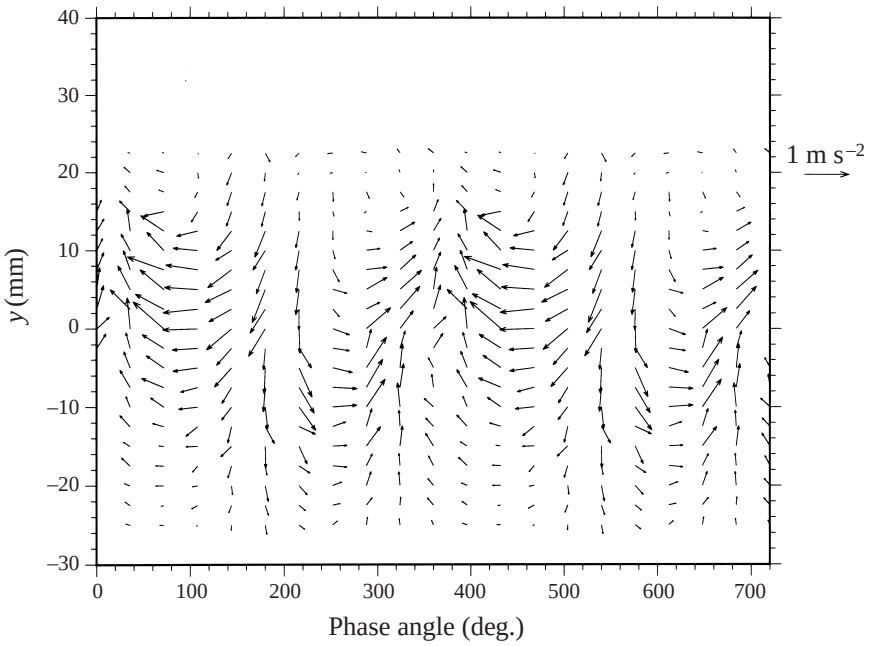

FIGURE 16. Local acceleration, $D\boldsymbol{u}_w/Dt \approx \boldsymbol{u}_w \cdot \nabla \boldsymbol{u}_w$, for $x/\lambda = 1.25$ for the carrier phase velocity field presented in figure 14.

core produces a large positive peak representing E_K generation within the carrier phase, resulting from an enhancement of the vertical settling of the bubble cloud within this region. The downwelling region upstream of the core represents a region of E_K destruction (where the E_P of the carrier phase is increasing) due to downward bubble motions. The free stagnation point is consistently situated in the region of transition between E_K destruction and generation – where there is essentially no energy redistribution.

At $x/\lambda = 1.25$, in the region above and downstream of the free stagnation point, a well developed downwelling is apparent, extending vertically somewhat beyond $y = 15\,\text{mm}$. However, in this area nearly zero energy redistribution is present, due to the presence of a still well-defined downwelling tongue of unladen fluid from the upper layer. The characteristics of the initial entrainment of the bubble cloud into the mixing region significantly impacts the vertical extent of the E_K destruction regions, more so than the adjacent E_K generation region associated with the upwelling of fluid from the lower stream.

The locations of the peaks of the E_K destruction regions move downward as the flow progresses downstream because of this impact of the initial entrainment characteristics on these regions. This is due to the fact that the well-defined regions of downwelling are confined more and more to positions beneath the vortex core as the flow evolves. Because of this, and the homogenization of the void fraction field, the E_K destruction peak at the $x/\lambda = 2.50$ station is located within the middle of the depleted sublayer noted in the analysis of the time-averaged attenuation profiles. The shape, location and peak values of the E_K generation regions on the downstream side of the Kelvin–Helmholtz billows remain similar to each other as the flow progresses downstream – except in their lateral extent, which grows as the mixing layer evolves.

The regions of E_K generation both occupy greater regions of the flow field and

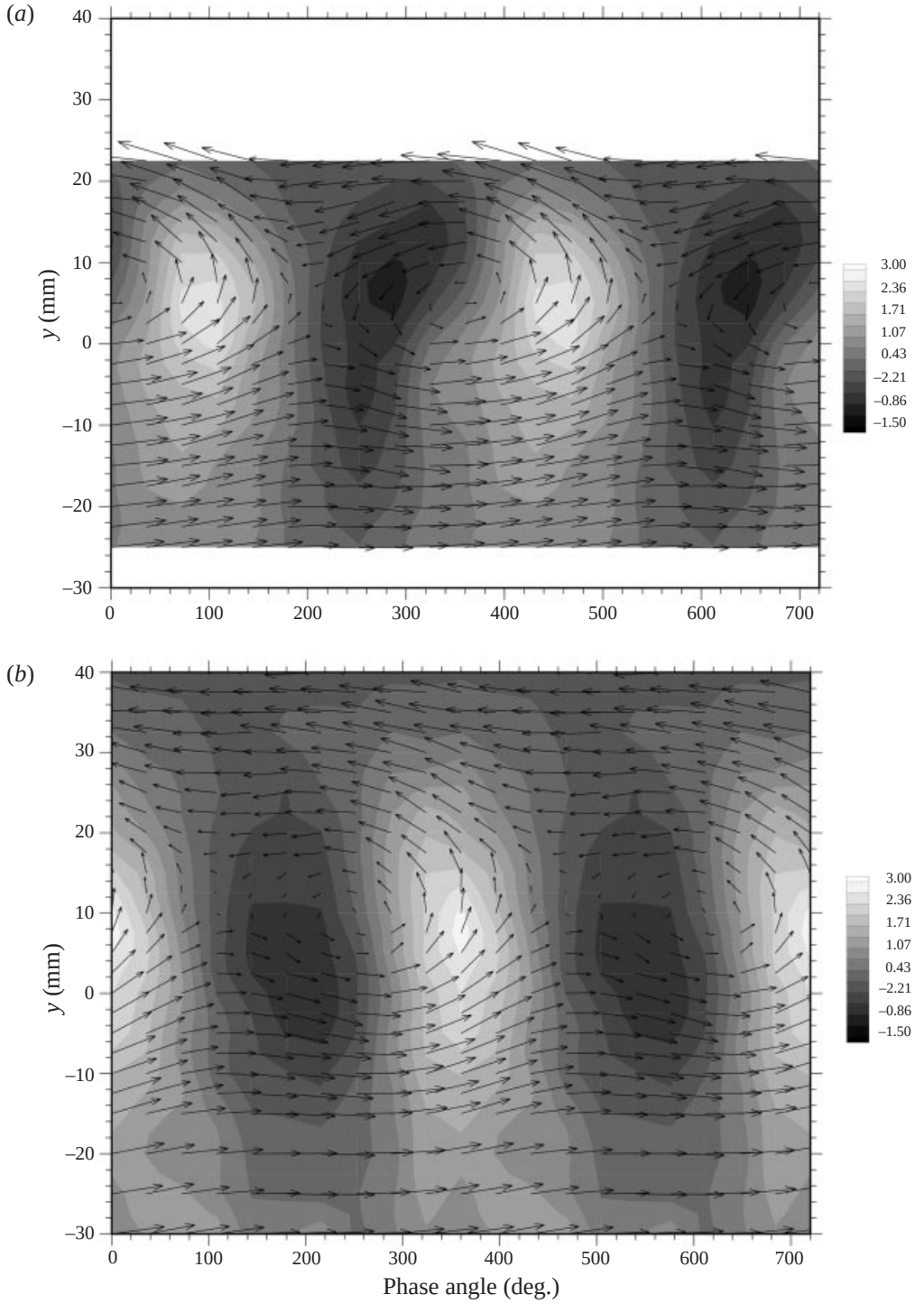

FIGURE 17. Phase-averaged total energy redistribution, $\rho_w \alpha_b (\mathrm{D}\boldsymbol{u}_w/\mathrm{D}t - \boldsymbol{g}) \cdot \boldsymbol{u}_w$, contours (mW m^{-3}) and carrier-phase velocity field for (*a*) $x/\lambda = 1.25$ and (*b*) $x/\lambda = 2.50$. The layer's mean streamwise velocity of 17 cm s^{-1} has been subtracted from the velocity fields.

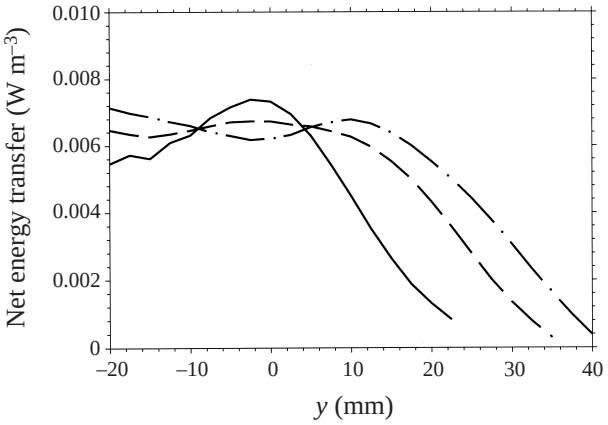

FIGURE 18. Net energy redistribution per period computed by integrating the total energy redistribution over one period for each measured cross-stream position: ——, $x/\lambda = 1.25$; — —, $x/\lambda = 1.88$; and — · —, $x/\lambda = 2.5$.

have peak values nearly three times those of the E_K destruction. The fact that E_K generation dominates E_K destruction on average in the flow is apparent when averaging the energy redistribution over one period, which is presented in figure 18. This averaging estimates the net time-averaged energy redistribution within the carrier phase due to the presence of the bubble cloud. Relatively early in the flow evolution (at $x/\lambda = 1.25$), while the initial inhomogeneities associated with the fluid entrainment processes are well-defined and after the enhanced bubble dispersion present from $0.63 < x/\lambda < 1.88$ has been allowed to evolve for only a short distance, the net energy redistribution displays a prominently peaked profile. This peak value occurs beneath the cross-stream position of the core of the Kelvin–Helmholtz billow. The rapid increase from the free stream is due to the development of the cross-stream velocity component and the fact that a significant void fraction of bubbles is present near to the lower free stream. The decline in net energy transfer in the region above $y = 0$ mm results from both a lower average void fraction in this region as well as the existence of the peak of E_K destruction located at $y \approx 10$ mm (see figure 17). The peak of the net energy redistribution is also somewhat below the cross-stream position of the peak value of RMS and is only about one-quarter of the way into the mixing region as evidenced by the mean streamwise velocity profiles.

Due to the downward evolution of the E_K destruction regions, the strong peak in the net energy redistribution has eroded by the $x/\lambda = 1.88$ measurement location. In fact, by the $x/\lambda = 2.50$ station, the cumulative effects of this downward movement along with the growth of the depleted sublayer adjacent to the lower free stream result in a local minimum in the net energy redistribution well below the core of the vortical structures.

The contribution to the overall energy redistribution of each size class is presented in figure 19. Because of the cubic dependence of displaced volume on bubble diameter, the smallest size class contributes very little to the total, even though it is the most numerous of the size classes. The contribution of the largest size class is confined to somewhat larger cross-stream values than that of the intermediate size class.

For bubbles (where the net force must vanish due to the lack of inertia) the balance of forces enables the computation of the carrier-phase energy redistribution solely from the force on the bubble resulting from the ambient flow field. From (4.8), the

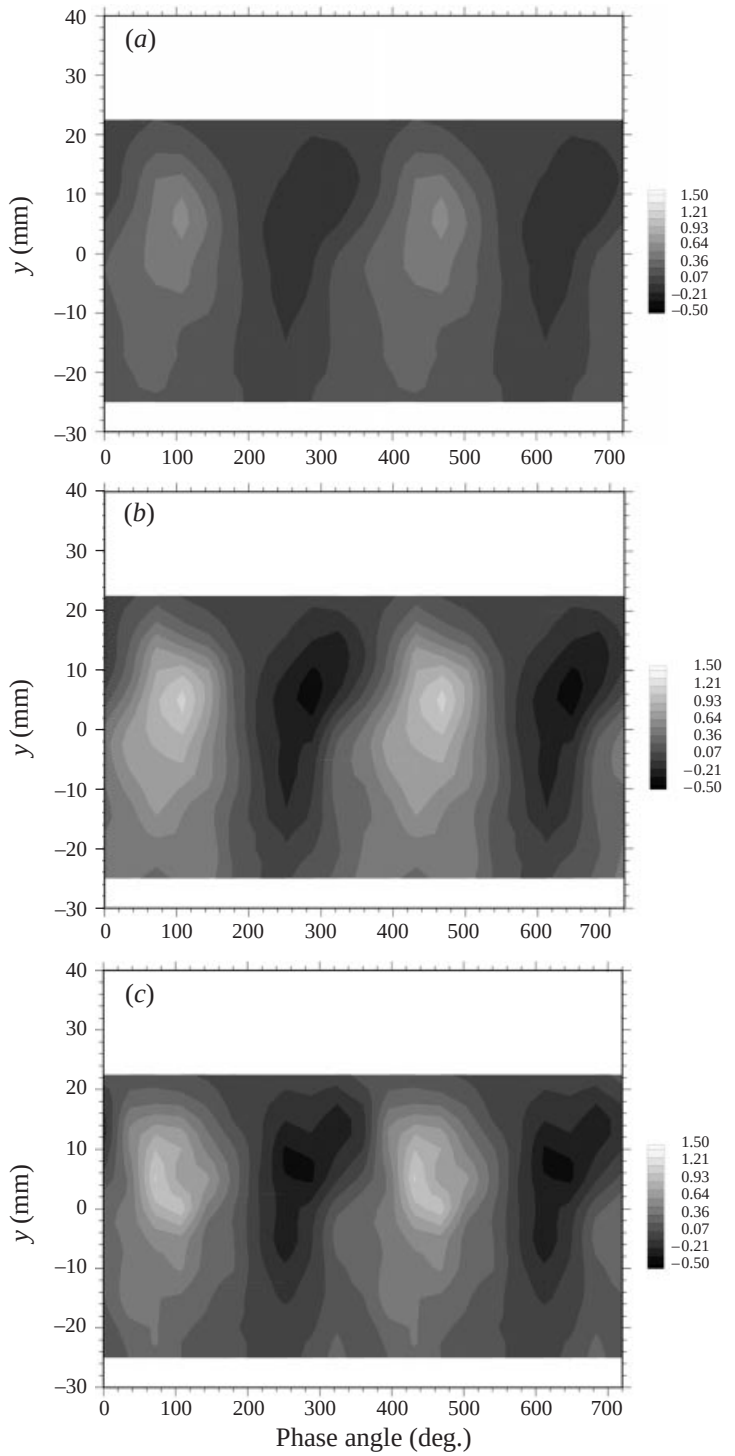

FIGURE 19. Contours (mW m^{-3}) showing the influence of each size class on total energy redistribution for $x/\lambda = 1.25$ for (*a*) size class 1: $\overline{D}_b \approx 27\,\mu$m, (*b*) size class 2: $\overline{D}_b \approx 44\,\mu$m, and (*c*) size class 3: $\overline{D}_b \approx 81\,\mu$m.

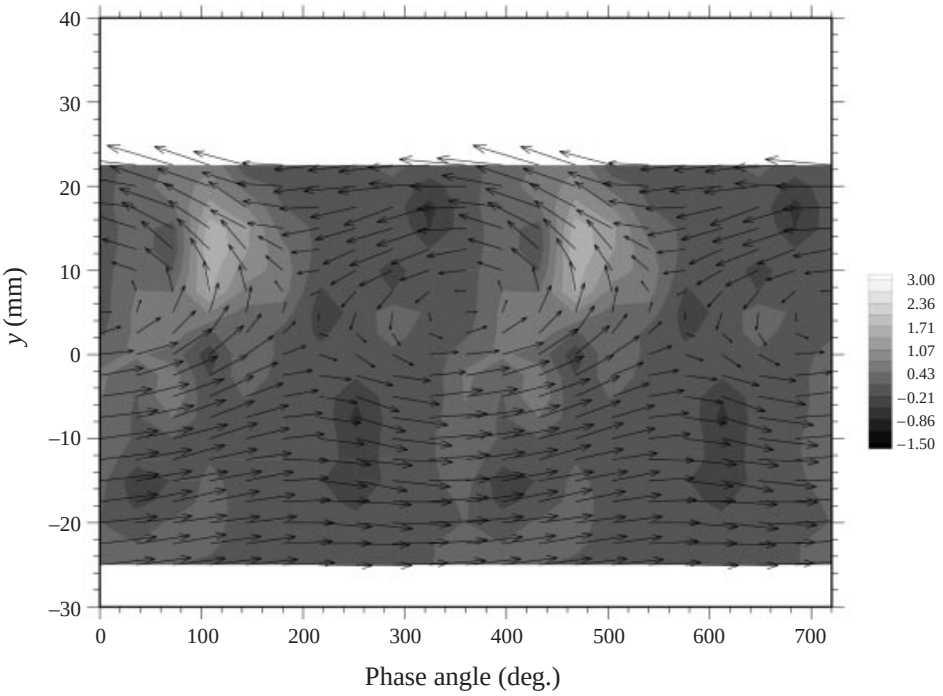

FIGURE 20. Energy redistribution contours resulting from the drag force ($\mathrm{mW\,m^{-3}}$), $(2\alpha_i\mu_w/D_i^2)(\boldsymbol{u}_i - \boldsymbol{u}_w)\cdot\boldsymbol{u}_w$, and the carrier-phase velocity field for $x/\lambda = 1.25$. The layer's mean streamwise velocity of $17\,\mathrm{cm\,s^{-1}}$ has been subtracted from the velocity field.

form of the interphase momentum transfer integral comes from the force resulting from the disturbance flow around the bubble (i.e. from the relative motion between the phases). From (4.10), we see that this disturbance flow force is composed of contributions from the quasi-steady Stokes drag, the added mass and Basset history forces. In this section, we consider only the contribution of the quasi-steady drag force to the overall energy redistribution. The form of this term for an individual bubble is

$$\boldsymbol{f}'_{\mathrm{Drag}}\cdot\boldsymbol{u}_w = 3\pi D_b\mu_w(\boldsymbol{u}_b - \boldsymbol{u}_w)\cdot\boldsymbol{u}_w. \tag{4.19}$$

The mesoscale-averaged value for this contribution is expressed as a summation over all bubbles in the averaging volume. We estimate the number of bubbles at each cross-stream position and phase angle through the local void fraction, volume fraction of the given size class and the average bubble size of that class:

$$\boldsymbol{F}'_{\mathrm{Drag}}\cdot\boldsymbol{u}_w = 3N_i\pi D_i\mu_w(\boldsymbol{u}_i - \boldsymbol{u}_w)\cdot\boldsymbol{u}_w = \frac{2\alpha_i\mu_w}{D_i^2}(\boldsymbol{u}_i - \boldsymbol{u}_w)\cdot\boldsymbol{u}_w. \tag{4.20}$$

Here the number of bubbles of size class i per unit volume, N_i, has been estimated by taking $N_i = \alpha_i/(\frac{1}{6}\pi D_i^3)$ and $D_i = D_{30_i}$. For a bubble rising in a still fluid (at its terminal rise velocity), the rate of conversion of E_P to E_K within the carrier fluid ($\boldsymbol{f}\cdot\boldsymbol{u}_w$) must be equal to that due to the drag term alone ($3\pi D_b\mu_w(\boldsymbol{u}_b - \boldsymbol{u}_w)\cdot\boldsymbol{u}_w$) due to the balance between the buoyancy and drag forces – all other terms vanishing. However, this one-to-one correspondence of the total energy redistribution and that due to the drag term alone does not exist in more complicated flow situations where other forces resulting from the disturbance flow can become significant.

The resulting estimate of the contribution of the quasi-steady drag term alone is presented in figure 20. Comparing with figure 17, we see that the peak values of the total energy redistribution and that resulting from the drag force alone are of similar magnitudes. However, the peak associated with E_K energy generation due to the drag term is significantly smaller in extent than the peak of total energy redistribution. It also can account for only the uppermost portion of the total E_K generation region. This result suggests that the terms in the equation of motion of the individual bubbles resulting from the disturbance flow are not dominated by the quasi-steady drag.

The contribution to the energy redistribution resulting from the quasi-steady drag force alone for each size class is presented in figure 21. The most striking feature is that the largest contribution to the total drag force estimate comes from the smallest size class. From (4.20), we see that the dependence of N_i is inversely proportional to D_i^2 and that the drag contribution of each size class goes as N_i. Therefore, even though we have seen that the contribution from the drag term accounts for the total energy redistribution in some regions of the flow field, we see that this holds only for the smallest size class because of its much greater population density.

5. Conclusions

The dispersion field of a dilute dispersed microbubble cloud interacting with a perturbed planar free-shear layer – as well as the interphase momentum and energy transfer – has been examined in detail experimentally for the first time. This study has investigated the role of the large, coherent structures known to dominate the entrainment and mixing within the shear layer in the dispersion and interphase energy transfer processes.

The evolution of the bubble cloud (i.e. void fraction) dispersion field is dominated by the influence of the large-scale coherent structures of the flow. The initial development is characterized by the entrainment processes of these large scales with significant inhomogeneities occurring due to the movement of high- and low-speed fluid into the layer. As this pattern evolves downstream and is smeared away by the relative motion of the two phases, a depleted sublayer forms in the void fraction field, resulting from the overturning of the large scales. At intermediate downstream distances, the lateral spreading of the dispersion field is greater than that of the streamwise velocity profiles superimposed with the rise rates of the individual bubbles. This region is followed by one in which the lateral spreading can be explained simply by the growth rate of the carrier phase together with the individual bubble rise rates. Little increase in the void fraction of bubbles at the stable accumulation point near the cores of the coherent structures is found, along with no segregation of the bubbles by size. The former effect is due to the relatively diffuse concentration of vorticity within the large scales.

This study has been restricted to relatively low free-stream void fractions in a flow without localized regions of high void fractions. This has allowed us to analyse the problem as a dilute dispersed flow, as well as allowing us to bring a powerful set of optical diagnostics to bear in interrogating the flow. For regions of high void fractions, the analysis as well as the instrumentation used in this study would be inadequate.

An analysis in the limit of such a dilute dispersed cloud of microbubbles, applied to the volume-averaged (i.e. mesoscale) equations of motion of the carrier phase, has provided the form of the interphase momentum transfer integral, and hence the E_K transfer terms. The simplifications for a massless dispersed phase (bubbles) have resulted in a form of the interphase momentum transfer integral that can be measured experimentally – which includes the cumulative influence of all terms in the equation

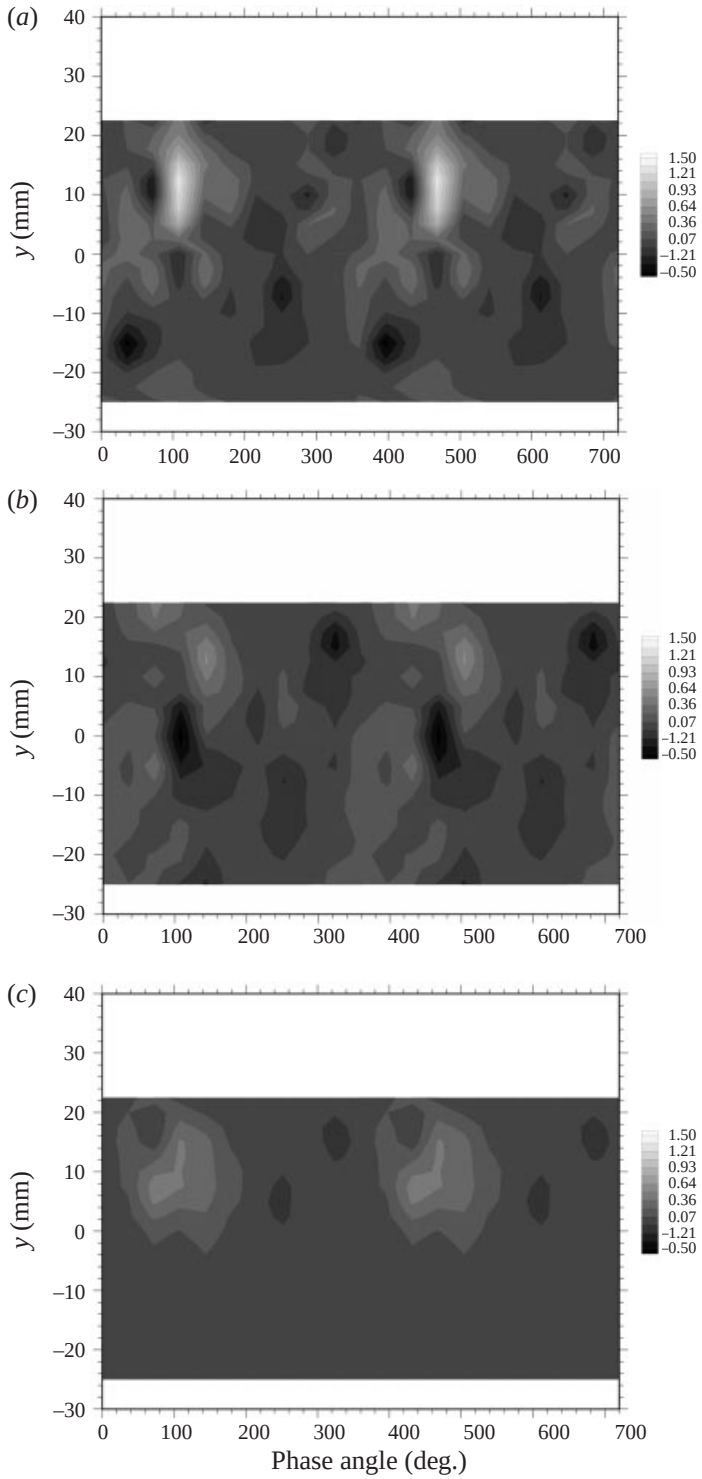

FIGURE 21. Contours ($\mathrm{mW\,m^{-3}}$) showing the influence of each size class on energy redistribution due to quasi-steady drag force for $x/\lambda = 1.25$ for (*a*) size class 1: $\overline{D}_b \approx 27\,\mu\mathrm{m}$, (*b*) size class 2: $\overline{D}_b \approx 44\,\mu\mathrm{m}$, and (*c*) size class 3: $\overline{D}_b \approx 81\,\mu\mathrm{m}$.

of motion of the bubble resulting from its relative motion with respect to the carrier phase.

The E_K redistribution within the carrier phase due to the presence of the bubble cloud occurs inhomogeneously across the mixing layer. Large peaks of E_K generation are associated with the upwelling regions downstream of the vortex cores. These peak values are typically located slightly beneath the peak values of the streamwise velocity RMS profiles. Weaker peaks of E_K destruction are associated with the downwelling regions upstream of the vortex cores. The locations of these latter peaks move downward from above the cross-stream of the vortex core to below it as the flow evolves downstream. The E_K generation regions are found to dominate at every downstream location, with the mean profiles of the net E_K generation per period initially peaking well beneath the region of highest carrier-phase velocity RMS. Downstream evolution of these profiles is characterized by the enhanced spreading of the void fraction field and the strengthening of the depleted sublayer adjacent to the lower free stream. The contribution of the quasi-steady drag term to the overall energy redistribution is seen to be dominant in only a limited region of the flow field, showing the well-documented importance of the other terms of the equation of motion of massless particles.

The authors would like to thank the assistance of Professors Ken Kiger and Carlos Martinez. This work was supported by the ONR under grant number #N00014-91-J-1252.

REFERENCES

Aerometrics 1994 *Phase Doppler Particle Analyzer User's Manual.* Sunnyvale: Aerometrics, Inc.

Antonia, R. A. 1981 Conditional sampling in turbulence measurement. *Ann. Rev. Fluid Mech.* **13**, 131–156.

Auton, T. R. 1987 The lift force on a spherical body in a rotational flow. *J. Fluid Mech.* **183**, 199–218.

Browand, F. K. & Latigo, B. O. 1979 Growth of the two-dimensional mixing layer from a turbulent and nonturbulent boundary layer. *Phys. Fluids* **22**, 1011–1019.

Browand, F. K. & Weidman, P. D. 1976 Large scales in the developing mixing layer. *J. Fluid Mech.* **76**, 127–144.

Brown, G. L. & Roshko, A. 1974 On density effects and large structure in turbulent mixing layers. *J. Fluid Mech.* **64**, 775–816.

Clift, R., Grace, J. R. & Weber, M. E. 1978 *Bubbles, Drops and Particles.* Academic.

Corrsin, S. & Lumley, J. 1956 On the equation of motion for a particle in turbulent fluid. *Appl. Sci. Res.* **6**, 114–116.

Dahm, W. J. A. & Dimotakis, P. E. 1987 Measurement of entrainment and mixing in turbulent jets. *AIAA J.* **25**, 1216–1223.

Detsch, R. M. 1991 Small air bubbles in reagent grade water and seawater 1. rise velocities of 20- to 1000-μm-diameter bubbles. *J. Geophys. Res.* **96** (C5), 8901–8906.

Dimotakis, P. E. 1987 Two-dimensional shear-layer entrainment. *AIAA J.* **25**, 1791–1796.

Drew, D. A. 1983 Mathematical modeling of two-phase flow. *Ann. Rev. Fluid Mech.* **15**, 261–291.

Druzhinin, O. A. & Elghobashi, S. 1998 Direct numerical simulations of bubble-laden turbulent flows using the two-fluid formulation. *Phys. Fluids* **10**, 685–697.

Elghobashi, S. E. & Abou-Arab, T. W. 1983 A two-equation turbulence model for two-phase flows. *Phys. Fluids* **26**, 931–938.

Elghobashi, S. E. & Truesdell, G. C. 1993 On the two-way interaction between homogeneous turbulence and dispersed solid particles. i: turbulence modification. *Phys. Fluids* A **5**, 1790–1801.

Hjelmfelt, A. T. & Mockros, L. F. 1966 Motion of discrete particles in a turbulent fluid. *Appl. Sci. Res.* **16**, 149–161.

Ho, C.-M. & Huerre, P. 1984 Perturbed free-shear layers. *Ann. Rev. Fluid Mech.* **16**, 365–424.

Hussain, A. F. & Zedan, M. F. 1978 Effects of the initial condition on the axisymmetric free-shear layer: Effects of the initial momentum thickness. *Phys. Fluids* **21**, 1100–1112.

Hussain, A. K. M. F. & Zaman, K. B. M. Q. 1980 Vortex pairing in a circular jet under controlled excitation. Part 2. Coherent structure dynamics. *J. Fluid Mech.* **101**, 493–544.

Kiger, K. T. 1995 Particle dispersion and inter-phase kinetic energy transfer in a turbulent, two-phase shear layer. PhD thesis, University of California, San Diego.

Kiger, K. T. & Lasheras, J. C. 1995 Effect of vortex pairing on particle dispersion and kinetic energy transfer in a two-phase turbulent shear layer. *J. Fluid Mech.* **302**, 149–178.

Kiger, K. T. & Lasheras, J. C. 1997 Dissipation due to particle/turbulence interaction in a two-phase, turbulent, shear layer. *Phys. Fluids* **9**, 3005–3023.

Lance, M. & Bataille, J. 1991 Turbulence in the liquid phase of a uniform bubbly air-water flow. *J. Fluid Mech.* **222**, 95–118.

Lasheras, J. C., Cho, S. & Maxworthy, T. 1986 On the origin and evolution of streamwise vortical structures in a plane, free-shear layer. *J. Fluid Mech.* **172**, 231–285.

Lázaro, B. J. 1989 Particle dispersion in turbulent free-shear flows. PhD thesis, University of Southern California.

Lázaro, B. J. & Lasheras, J. C. 1992*a* Particle dispersion in the developing free-shear layer. Part 1. Unforced flow. *J. Fluid Mech.* **235**, 143–178.

Lázaro, B. J. & Lasheras, J. C. 1992*b* Particle dispersion in the developing free-shear layer. Part 2. Forced flow. *J. Fluid Mech.* **235**, 179–221.

Liepmann, H. W. & Laufer, J. 1947 Investigations of free turbulent mixing. *NACA Tech. Note* 1257.

Lovalenti, P. M. & Brady, J. F. 1993 The force on a sphere in a uniform flow with small-amplitude oscillations at finite Reynolds number. *J. Fluid Mech.* **256**, 607–614.

Lumley, P. 1976 *Turbulence*, chap. 47. Springer.

Maxey, M. & Riley, J. J. 1983 Equation of motion for a small rigid sphere in a nonuniform flow. *Phys. Fluids* **26**, 883–889.

Maxey, M. R., Chang, E. J. & Wang, L.-P. 1994 Simulation of interactions between microbubbles and turbulent flows. *Appl. Mech. Rev.* **47** (6), S70–S74.

Mei, R. 1992 An approximate expression for the shear lift force on a spherical particle at finite Reynolds number. *Intl J. Multiphase Flow* **18**, 145–147.

Mei, R. & Adrian, R. J. 1992 Flow past a sphere with an oscillation in the free-stream velocity and unsteady drag at finite Reynolds numbers. *J. Fluid Mech.* **237**, 323–341.

Mei, R., Adrian, R. J. & Hanratty, T. J. 1991 Particle dispersion in isotropic turbulence under stokes drag and basset force with gravitational settling. *J. Fluid Mech.* **225**, 481–495.

Monkewitz, P. A. & Huerre, P. 1982 Influence of the velocity ratio on the spatial instability of mixing layers. *Phys. Fluids* **25**, 1137–1143.

Rightley, P. M. 1995 Bubble dispersion and interphase coupling in a free shear flow. PhD thesis, University of California, San Diego.

Rightley, P. M. & Lasheras, J. C. 1996 Experimental study of a bubbly, turbulent, free-shear layer. *Twentieth Symp. on Naval Hydrodynamics*, pp. 766–775. National Academy Press.

Ruetsch, G. R. & Meiburg, E. 1993 On the motion of small spherical bubbles in two-dimensional vortical flows. *Phys. Fluids* **5**, 2326–2341.

Ruetsch, G. R. & Meiburg, E. 1994 Two-way coupling in shear layers with dilute bubble concentrations. *Phys. Fluids* A **6**, 2656–2670.

Saffman, P. G. 1985 The lift on a small sphere in a slow shear flow. *J. Fluid Mech.* **22**, 385–400.

Schowalter, D. G. 1993 The effect of stable stratification on three-dimensional structure in shear layers. PhD thesis, University of California, San Diego.

Sene, K. J., Hunt, J. C. R. & Thomas, N. H. 1994 The role of coherent structures in bubble transport by turbulent shear flows. *J. Fluid Mech.* **259**, 219–240.

Siegel, R. & Howell, J. R. 1981 *Thermal Radiation Heat Transfer*, 2nd edn. Hemisphere.

Soo, S. L. 1989 *Particulates and Continuum: Multiphase Fluid Dynamics*. Hemisphere.

Squires, K. D. & Eaton, J. K. 1990 Particle response and turbulence modification in isotropic turbulence. *Phys. Fluids* A **2**, 1191–1203.

Sridhar, G. & Katz, J. 1993 Lift and drag forces on bubbles entrained by a vortex ring. ASME FED vol. 153, pp. 165–170.

Tio, K.-K. & Lasheras, J. C. 1993 The dynamics of a small spherical particle in steady, two-dimensional vortex flows. *AIAA Paper* 93-187.

Tio, K.-K., Lasheras, J. C., Gañàn-Calvo, A. & Liñàn, A. 1993*a* The dynamics of bubbles in periodic vortex flows. *Appl. Sci. Res.* **51**, 285–290.

Tio, K.-K., Liñán, A., Lasheras, J. C. & Gañán-Calvo, A. M. 1993*b* On the dynamics of buoyant and heavy particles in a periodic stuart vortex flow. *J. Fluid Mech.* **254**, 671–699.

Turner, J. S. 1973 *Buoyancy Effects in Fluids*. Cambridge University Press.

Van de Hulst, H. C. 1957 *Light Scattering by Small Particles*. Dover.

Viollet, P. L. & Simonin, O. 1994 Modelling dispersed two-phase flows: Closure, validation and software development. *Appl. Mech. Rev.* **47** (6), S80–S84.

Weisbrot, I., Einav, S. & Wygnanski, I. 1982 The nonunique rate of spread of the two-dimensional mixing layer. *Phys. Fluids* **25**, 1691–1693.

Williams, F. 1960 Progress in spray-combustion analysis. *Eighth Symp.* (*Intl*) *on Combustion*, pp. 50–69. The Combustion Institute.

Winant, C. C. & Browand, F. K. 1974 Vortex pairing: the mechanism of turbulent mixing-layer growth at moderate reynolds number. *J. Fluid Mech.* **63**, 237–255.

Wygnanski, I. & Fiedler, H. E. 1970 The two-dimensional mixing region. *J. Fluid Mech.* **41**, 327–361.